Physics – Uspekhi **64** (1) 3 – 27 (2021)

REVIEWS OF TOPICAL PROBLEMS PACS numbers: 07.55.Jg, **75.70. – i, 85.75. – d**

Measurements of the magnetic properties of conduction electrons

V M Pudalov

DOI: https://doi.org/10.3367/UFNe.2020.05.038771

Contents

Abstract. We consider various methods and techniques that are used in experimental condensed matter physics for measuring electron magnetization and susceptibility. The list of considered methods for macroscopic measurements includes magnetomechanical, electromagnetic, modulation-type, and thermodynamic methods based on chemical potential variation measurements. We also consider local methods of magnetic measurements based on the spin Hall effect and nitrogen-substituted vacancies (NV centers). Scanning probe magnetometers–microscopes are considered, such as the magnetic resonance force microscope, SQUID microscope, and Hall microscope. The review focuses on the electron spin magnetization measurements in nonmagnetic materials and systems, particularly in low-dimensional electron systems in semiconductors and in nanosystems that have come to the forefront in recent years.

Keywords: spin magnetization, spin susceptibility, conduction electrons, measurements of magnetic properties

1. Introduction

Due to the additivity of thermodynamic quantities, measurements of any of them become challenging upon reducing the size of the studied sample. Experimentalists already face this problem when dealing with small three-dimensional objects such as 'whiskers' of Zn, Bi, and Sn, whose typical sizes are $1 \times 10 \times (100-1000)$ μm^3. Indeed, the magnetic susceptibility of nonmagnetic metals is typically $\sim 10^{-6}$; therefore, the magnetization of such a sample in a field of 10^3 Oe is $\sim 10^{-12}$ CGS, which is several orders of magnitude less than the sensitivity threshold of traditional laboratory magnetometers, including torsion [1, 2], Faraday (or 'magnetic balance'), vibration-type (so-called Foner magnetometers) [3], and others.

For such small samples, a change in the magnetic susceptibility by 1% in a field $B = 10^3$ G causes a change in the magnetic flux through the sample cross section of 1×10 μm^2 by about 10^{-11} CGS, which is approximately 10^{-4} times the flux quantum and also lies beyond the sensitivity threshold of SQUID magnetometers.

This seemingly purely technical problem for a long time remained an obstacle to studying the magnetic properties of two-dimensional (2D) electron systems in which the effective thickness of the electron layer is of the order of the Fermi wavelength $10-50$ Å and where the typical number of electrons in the sample in total is $10^8 - 10^9$. The characteristic energy associated with the desired changes in magnetic properties are not so small, $\sim \mu_B B \sim 0.1$ K per electron, where μ_B is the Bohr magneton. This obviously means that the difficulty of measuring the magnetic properties of 2D and ultrathin samples is associated not with the smallness of the effects but with the failure of traditional methods for measuring the properties of samples of small thicknesses.

Clearly, to overcome the problem, different measurement methods are needed in which the signal strength does not

V M Pudalov Lebedev Physical Institute, Russian Academy of Sciences, Leninskii prosp. 53, 119991 Moscow, Russian Federation;
E-mail: pudalov@lebedev.ru

Received 4 October 2019, revised 2 May 2020
Uspekhi Fizicheskikh Nauk **191** (1) 3 – 29 (2021)
Translated by V M Pudalov and A M Semikhatov

decrease proportionally to the sample volume. This review addresses a number of such, in fact, classical methods that have been successfully used in practice.

In the field of condensed matter magnetometry, there is a review by Usher and Elliot [4] discussing classical methods for measuring orbital electron magnetization and their application for studying the quantum Hall effect and related phenomena. There are also a number of monographs (e.g., [5]) where techniques for measurements with ferromagnetic materials are considered. In this review, in contrast to [4, 5], we focus on methods for measuring *spin* rather than orbital magnetization of electrons in *nonmagnetic* materials; spin magnetization is usually much less than the orbital one. For completeness and the convenience of the reader, we briefly mention not only spin magnetism but also the orbital magnetism of electron systems, including those that have already been described in [4]. However, we supplement this description with some results omitted in [4].

We then describe more modern methods developed in the last 20 years for studying the spin properties of strongly correlated electrons in low-dimensional systems. Recently, thermodynamic methods have turned out to be among the most fruitful; they are based on measurements of chemical potential derivatives for 2D systems. We describe several key physical results obtained by these methods. Finally, we consider local methods of measurements, including various types of scanning magnetic microscopes, booming recently in connection with the numerous problems in spintronics, single-spin manipulation, biophysics, and virology.

2. Traditional methods of electron magnetization measurements

2.1 Electromechanical methods

These methods can be divided into two classes: (a) based on measurements of the force acting on a sample in an inhomogeneous magnetic field, $\mathbf{F} = (\mathbf{M}\nabla)\mathbf{B}$ (Faraday magnetometer), or of the torque $\mathbf{L} = \mathbf{M} \times \mathbf{B}$ in the case of an anisotropic sample in a uniform magnetic field (a torsion magnetometer) and (b) based on electromagnetic induction measurements (a Foner magnetometer).

2.1.1 Torsion magnetometer. This type of magnetometer is based on 'torsion balance' introduced into everyday use of experimental physics at the end of the 18th century by C-A de Coulomb to measure electrical forces and by H Cavendish to measure gravitational forces. In contemporary experimental physics, laboratory magnetometers are ubiquitous for measuring the torque acting on an anisotropic sample in a uniform field **B**. In torsion magnetometers, this torque is compensated by forces from the elastic element deformation.

To measure the deformation of the elastic element, capacitive, inductive, or optical sensors are used. Capacitive deformation sensors [1], starting from the 1960s to the present, have been successfully used for measurements of oscillatory magnetization (de Haas–van Alphen effect, dHvA). With regard to the problem of measuring the magnetic properties of low-dimensional systems, torsion balance scales were adapted by Eisenstein et al. to measure the dHvA effect for electrons in a 2D system [6, 7]; the design of these scales is shown schematically in Fig. 1. The sample — a GaAs–AlGaAs heterostructure with the 2D electron gas —

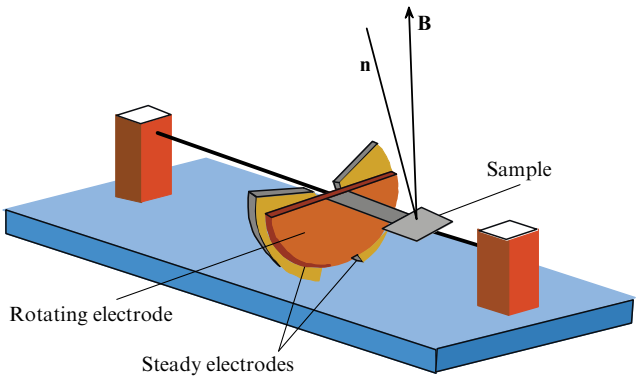

Figure 1. Schematic design of the torsion magnetometer from Ref. [6]. **n** — normal to the sample plane, **B** — magnetic field vector.

is attached to a thin elastic thread (Pt–W, with a diameter of 37 μm and 2 cm long), stretched perpendicular to the magnetic field direction. The orbital magnetic moment **M** of electrons in a 2D system is the partial derivative of the free energy with respect to the magnetic field:

$$\mathbf{M} = -\left[\frac{\partial F}{\partial \mathbf{B}}\right]_N .$$

For isotropic samples (ignoring the geometric demagnetizing factor), the field-induced magnetic moment **M** is parallel to **B**, and therefore torque does not arise. For a 2D electron system, the induced orbital moment is always directed normal to the 2D plane, due to in-plane cyclotron motion. This magnetic moment causes a mechanical torque acting on the sample,

$$\mathbf{L} = \mathbf{M} \times \mathbf{B} + \mathbf{d} \times \nabla(\mathbf{MB}) ,$$

where the second term arises in an inhomogeneous magnetic field and **d** is the vector arm of the applied torque relative to the rotation axis.

The torque **L** leads to twisting the elastic thread until the force of its elastic deformation compensates the applied torque. The thread rotation angle ϕ is registered, for example, by a capacitance change. For a small twisting angle $\varphi \ll \theta_0$, the restoring mechanical moment of the twisted elastic thread is $L_\varphi = MB\sin\theta_0$, where θ_0 is the angle between the field direction and the normal to the plane. While deviations from the equilibrium are small, $\varphi < 10^{-4}$ rad, torsion scales operate in the linear regime, with $\varphi \propto M$.

The authors of [6, 7] estimated the sensitivity limit for the thread twisting as 1 μrad, and for the magnetometer in total as 10^{-12} J T^{-1} (or 10^{-9} CGS) in a field of 5 T, which is equivalent to $10^{11}\mu_B$. To detect the dHvA effect with such a relatively low magnetometer sensitivity, the authors used a GaAs/AlGaAs heterostructure containing a large number of parallel-connected 2D electron sheets with a total area of 2 cm^2 [6], and even 12.5 cm^2 [7]. Due to the nonlinearity of capacitance changes with the angle (disc misalignment), the amplitude **M** was measured in Refs [6, 7] with a 25% uncertainty.

A different design of the torsion magnetometer with a capacitor more sensitive to the angle of sample rotation was developed by Templeton [8] and was later applied with some improvements in a number of studies [9–11]. In this design, twisting the thread together with the sample and the capacitor

plate changes the effective capacitor gap d rather than the area of the plates. As a result, relative capacitance changes amount to $\delta d/d$, rather than $\delta S/S$, as in the design in Fig. 1, giving a gain in threshold sensitivity by an order of magnitude.

Due to the small gap $d \approx 0.2$ mm between the capacitor plates, the magnetometer threshold resolution in terms of the rotation angle $(1/C)(\mathrm{d}C/\mathrm{d}\varphi)$ could be a factor of ≈ 25 better in this design than in the magnetometer in Fig. 1, although in practice it appeared to be improved only 10-fold, being limited by vibrations. Another advantage of this design is the possibility of using an electrostatic (ponderomotive) force, by applying a DC voltage between the capacitor plates. Such a feature is useful for damping the rotation system dynamics, for calibrating the absolute value of the elastic torque (in situ, in the course of experiment), as well as for introducing feedback, thereby linearizing the amplitude response characteristics of the magnetometer.

The threshold resolution was 10^{-12} J in terms of the detectable torque and ~ 1 μrad in units of the detectable rotation angle, or 10^{-5} in terms of the relative change in capacitance. This resolution enabled detecting dHvA oscillations for a single heterojunction 8 mm^2 in area, with a total number of electrons $\sim 7 \times 10^{10}$.

Because all torsion magnetometers are based on a freely suspended electromechanical system, the main source of noise is vibrations. Wiegers et al. [12, 13] described a design more resistant to vibrations, which contains a cylindrically symmetric rotor capacitor, with the sample located in the center of mass of the rotary unit.

These design features have reduced the parasitic coupling to external vibrations. The resonant frequency of the suspended system is 1.5 Hz, and the sensitivity threshold of this magnetometer can be estimated from the reported measurements of the oscillatory signal as $\delta M \sim 0.01\mu_\mathrm{B}$ per electron, although slow variations in the background were about a factor of 10 larger [12, 13]. The authors estimated the threshold magnetometer sensitivity as 10^{-13} J T^{-1}, which is equivalent to $\delta M = 10^{10}\mu_\mathrm{B}$ in a field of 1 T.

2.1.2 Torsion magnetometers with optical detection. In torsion magnetometers with capacitive sensors, the detecting bridge circuit is fed with a low-frequency AC voltage, which can induce unwanted EMF at the sample contacts.

In Refs [14, 15], an optical technique was used to detect sample deviations. For this, a laser beam was introduced into a cryostat via a multimode fiber and reflected from the sample, after which it reached the photodetector. In [16], the magnetometer was successfully used to measure electron magnetization of quasi-two-dimensional small organic crystals (weighing 0.13 mg), as well as to measure magnetization of GaAs double quantum wells [15] and a single-layer GaAs/AlGaAs heterostructure [14]. A threshold sensitivity of 2×10^{-13} J T^{-1} in a field of 15 T corresponds to magnetization changes $\delta M = 5 \times 10^{-3}\mu_\mathrm{B}$ per electron. Optical detection turned out to be workable even for measurements in the field of a Bitter magnet, which creates fairly large electrical noise. In this case, the threshold sensitivity was an order of magnitude worse, but was still sufficient for studying quantum oscillations of magnetization of single- [16] and double-layer heterojunctions GaAs/AlGaAs [15].

2.1.3 Microconsole-type magnetometers. The operation principle of these magnetometers is similar to the torsion balance. Just as in the latter, the torque acting on a sample from the magnetic field is balanced by the mechanical torque of elastic forces. The difference is that the elastic element undergoes bending rather than torsion deformation.

In Ref. [17], a 'flexural' magnetometer is described in which the sample is not integrated into the console, but itself plays the role of a bending element. Thus, the torque acting on the sample causes bending of the sample itself, and not of the auxiliary elastic element. The sample — a flat threadlike crystal (whisker) ≈ 1 μm thick and $l \approx 200-1000$ μm long — is placed in a magnetic field tilted by $0 < \varphi < 90°$ relative to its plane. One end of the sample is firmly fixed. The magnetic field induces the torque $\mathbf{L} = \nabla_\varphi(\mathbf{MB})$. According to the elasticity theory, the resulting bending of the sample is characterized by a certain average angle

$$\alpha = \kappa \frac{Ll}{Ed^3 b}\,, \tag{1}$$

where E is the elastic modulus, d is the thickness, b is the sample width, and κ is a factor of the order of unity.

As can be seen from Eqn (1), the bending angle is inversely proportional to d^3, while the torque L itself is proportional to the sample volume, i.e., the thickness d. Thus, with a decrease in the sample thickness, the bending angle does not decrease, but increases! The measured bending angle is a measure of the mechanical torque $\mathbf{L}$, and therefore of the magnetic moment $\mathbf{M}$.

Using this magnetometer, quantum magnetization oscillations were measured for a threadlike Bi crystal with sizes of $1 \times 10 \times 600$ μm^3 [18]. The bending angle for such samples in this case was 10^{-3} rad, and magnetic moment changes 10^{-11} CGS.

To linearize the characteristics of the device, feedback is introduced by applying a voltage U between the sample and a closely located metal plate. The torque ηU^2 of electrostatic forces acting on the sample compensates the measured torque L. For a large amplification factor in the feedback circuit, the angle α is practically unchanged, and ηU^2 is the measure of the desired magnetization signal $\mathrm{d}M/\mathrm{d}\varphi$. Due to the feedback, the dynamic range of the measured moment spanned 4 orders of magnitude, i.e., 80 dB [18]. The noise level of the magnetometer was $\sim (10^{-6}-10^{-7})$ dyn cm in the 1 Hz bandwidth.

With the development of microtechnologies at the end of the 20th century, micromechanical cantilever (or console) magnetometers (MCMs) were designed based on both silicon technology [19, 20] and GaAs technology [21, 22]. Figure 1 shows a planar sample with the 2D electron gas, mounted at the end of an elastic microconsole. The external magnetic field $\mathbf{B}$ is applied at an angle to the sample plane (Fig. 2). Because the orbital electron magnetization vector is perpendicular to the 2D electron gas plane, the console with the sample experiences the mechanical torque $\mathbf{L} = \mathbf{M} \times \mathbf{B}$. Thus, the desired magnetic moment, in the first approximation, is proportional to the angle of deformation of the elastic beam.

The operation principle of the MCM is illustrated in Fig. 2 taken from [20]: the sample, glued at the end of the console, is a chip 1 mm^2 in area with an Si/SiGe heterojunction containing a 2D electron system; to reduce the weight, the SiGe substrate is thinned to 10 μm. The console with the sample is directed at an angle α to the magnetic field $\mathbf{B}$ vector; changes in the magnetic moment, proportional to the torque L, are directly related to the console bending angle:

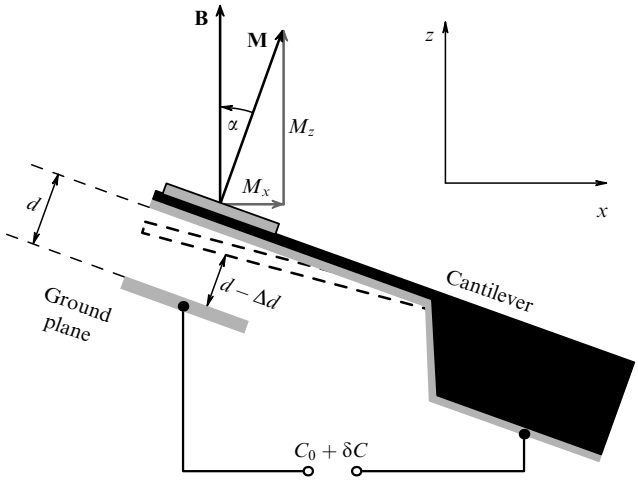

Figure 2. Schematic design of a microconsole magnetometer [20].

$\delta M = \delta L / B_\perp \tan\alpha$. The typical thickness of the bending element — beam — is 10 μm [22].

Micro-console magnetometers provide high sensitivity. In particular, in Ref. [22], the threshold sensitivity was $\delta M \approx 3 \times 10^{-15}$ J T^{-1} ($\delta L \approx 1 \times 10^{-14}$ N m) or $\sim 10^7 \mu_B$, i.e., $10^{-3}\mu_B$ per electron. In experiment [20], using this magnetometer, quantum magnetization oscillations for a 2D electron system in SiGe were reliably detected starting from a field ~ 1 T. Using this, in Ref. [20], the authors were able to study Landau level broadening, the valley and spin splittings and their renormalization in a magnetic field. In experiments [23, 24] with a GaAs/AlGaAs heterojunction, the authors measured the density-of-states profile at the Landau levels: minima of the density of states, the amplitude of oscillations in absolute units, as well as the enhancement of spin splitting caused by exchange interaction between the Landau levels. In an experiment with $ZnSe/Zn_{1-x-y}Cd_xMn_ySe$ quantum wells [25], the evolution of extended states at the Landau levels with level broadening was studied.

In most magnetometers [19, 20, 22, 23], the bending of the micro-console was detected via changes in the capacitance of the capacitor, $C = C_0 + \delta C$, with a gap between the plates ranging from 100 μm [20] or 50 μm [23] to 0.1 μm [26].

Besides the capacitive method of measuring beam deformation, in a number of MCM designs [26, 27] an optical technique was used, similar to that considered above for torsion magnetometers. Relinquishing electrical measurements of capacitance with an AC current allows, in principle, eliminating cross interference on the sample and therefore enables measuring DC transport properties simultaneously with magnetization measurement.

For measurements of the magnetic moment for a ferromagnetic semiconductor $Ga_{1-x}Mn_xAs$ in [21], another method was used: measuring the shift of the vibration eigenfrequencies of the console. The elastic beam in the magnetometer [21] had transverse dimensions of 50×0.1 μm^2, a length of 400 μm, a resonant frequency ≈ 1600 Hz, and a Q-factor of 11500. A sample with dimensions of 40×100 μm^2 was installed at the end of the beam. With these parameters, the threshold sensitivity was shown to be $3 \times 10^6 \mu_B$ in a field of 0.1 T and in the 1 Hz bandwidth [21].

The obvious advantages of MCMs are their miniature design and short response time, which is due to the resonant frequency of the beam being approximately inversely proportional to its length. In practical constructions, the resonant frequency is ~ 1 kHz [19], allowing such magnetometers to be used in measurements in pulsed fields. Of course, for applications in 'long' pulsed magnetic fields, of the order of tens of ms, the mass of the sample should be small, of the order of a mg; generally, for static measurements, the mass is limited to ~ 10 mg, due to unbalanced gravity. In some of these devices [21, 22, 27], the micro-console is integrated into a single unit with the sample — a GaAs-based heterojunction substrate with a 2D electron gas.

It is worth noting a local magnetometry technique related to MCMs: the scanning magnetic force microscope (MFM), to be briefly considered in Section 5.3.1 below.

2.1.4 Vibrating-type magnetometer. In vibrating magnetometers (VMs), the measured signal is the EMF induced by mechanical vibrations of the sample relative to a pick-up coil, placed in a constant magnetic field. The VM was invented by Foner [28] and described by him in detail in Ref. [3]. In the original design [3, 28], the sample vibration was driven by a loudspeaker cone in the direction perpendicular to the magnetic field. The author estimated the threshold sensitivity in terms of the susceptibility as $\delta\chi/\chi \sim 2 \times 10^{-10}$ in the frequency bandwidth of 2×10^{-2} Hz [3] and in terms of magnetization as 10^{-9} CGS in a field of 1 T [29].

Various options of the pick-up systems for detecting the induced AC magnetic field, including SQUID magnetometers are discussed in review [29]. Various examples of VMs in cryostats with ^{3}He [30, 31] pumping, in dilution refrigerators [32], and in hydrostatic pressure cells [33, 34] are also considered. The 'inverse' VM design is described in [35], in which the sample is likewise placed in the bore between two coils. However, the coils are used not to receive the induced voltage but to generate an alternating magnetic field. As a result, a force acts on the sample causing it to vibrate, which is detected by piezo-sensors.

When superconducting coils are used (in contrast to an electromagnet with a gap between the magnet poles, as in the first studies [3, 28, 29]) in modern VMs [36–40], the sample moves parallel to the magnetic field of the solenoid, rather than perpendicular. Figure 3 shows a schematic design of the pick-up coil system for this geometry, called a 'vibrating sample magnetometer' (VSM).

Let a sample with a magnetic moment M be located at an average distance Z from the plane of the pick-up coil with radius r. The sample sizes are presumed to be much less than r and Z. The reciprocal motion of the sample along the magnetic field, $z(t) = Z_0 \sin(\omega t)$, induces an EMF in the pick-up coil [36–41]:

$$E \propto \frac{\partial \Omega}{\partial Z} = 6\pi r^2 Z \left(Z^2 + r^2\right)^{-5/2}, \qquad (2)$$

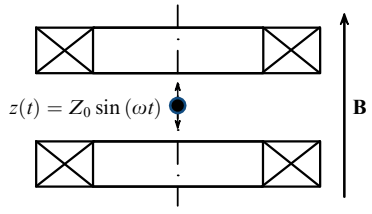

Figure 3. Schematics of pickup coils in a VSM for sample vibrations along the field.

where Ω is the angle subtended by the coil perimeter as seen from the sample location point, and the transverse dimensions of the coils are assumed to be much less than r and Z. For a pair of identical oppositely connected coils spaced $2Z$ apart along the solenoid axis, the sample deviation from the center by the distance x induces the EMF

$$E(Z,x) \propto 6\pi r^2 \left\{ (Z+x)\left[(Z+x)^2+r^2\right]^{-5/2} + (Z-x)\left[(Z-x)^2+r^2\right]^{-5/2} \right\}. \quad (3)$$

A detailed analysis of the EMF induced in the pick-up coils of various geometries and for their various locations is given in Ref. [40]. The amplitude of the induced voltage has a maximum at $Z = r/2$; however, to achieve the maximum flatness of $E(x)$ (which is weakly sensitive to the radial deviation of the sample middle point from the ideal position), $Z = \sqrt{3}r/2$ is usually chosen [36].

To drive the sample vibration, several techniques are now used: electric motors with lower gears [37], bimorph piezoelements [31], crankshaft mechanisms [38], and stepper motors [39]. The threshold sensitivity of a VSM typically ranges from $\sim 10^{-5}$ CGS [37, 39] to 10^{-6} CGS [31].

With an increase in the amplitude of oscillations, even harmonics appear in the picked-up EMF in the receiving coils. In Ref. [40], the amplitude of the second harmonic was used to absolutely calibrate the VSM; this method is conceptually similar to the one discussed below, that of finding the magnetization amplitudes for a nonlinear oscillator [42, 43].

Vibrating sample magnetometers have proven to be reliable and convenient tools and are currently produced by a number of manufacturers of scientific equipment [44].

2.1.5 Summary. The electromechanical and electromagnetic magnetometers described above provide the possibility of taking measurements of the thermodynamic magnetization $M = -\mathrm{d}F/\mathrm{d}B$ in absolute units. For the majority of them (except some console types [19]) magnetization measurements are performed under slow magnetic field sweeping or at a constant field. To lower the unwanted vibration effects, all these instruments have a low resonant frequency of their elastic mechanical system, ~ 1 Hz, and therefore field modulation is not used. As a result, the magnetometers are rather slow and, besides the oscillatory magnetization, detect an unwanted slow monotonic background signal, related to drifting environment parameters, the drifting of the construction and magnetism of its elements, etc. Despite all these shortcomings, due to the simplicity of the design, VSMs are widely used and are commercially available for laboratory applications.

Obviously, to reduce the effect of drift, it is necessary to increase the modulation frequency of the signal. The only parameter allowing fast modulation is the concentration of electrons, which can be changed in 2D structures by varying the gate voltage. This modulation method is described in Section 2.2.2 below.

2.2 Electromagnetic magnetometers

2.2.1 SQUID magnetometer. The first measurements of the quantum oscillations of magnetization for a 2D electron sheet were done in Refs [45, 46] using SQUID magnetometers. By now, a large number of laboratory instruments of this type have been described in the literature; moreover, SQUID magnetometers are commercially available; for this reason, we mention them here only briefly. In Refs [45, 46], the authors used a commercial SQUID magnetometer whose threshold sensitivity was insufficient for detecting quantum oscillations of a single 2D layer of electrons with a density $\sim 10^{11}$ cm^{-2}. For this reason, the authors used a set of 23 parallel GaAs–AlGaAs heterostructures, each with 173 2D layers (quantum wells), a total of 4000 parallel-connected 2D layers of 240 cm^2 in area. As a result, the authors for the first time observed quantum oscillations (de Haas–van Alphen effect) for a 2D electron system.

In a more advanced design [47], the threshold sensitivity was improved by more than three orders of magnitude; as a result, the authors registered quantum oscillatory magnetization for electrons in a GaAs–AlGaAs heterostructure 7 mm^2 in area. Subsequently, they were able to study electron magnetization in the fractional quantum Hall effect regime [48].

In a SQUID magnetometer [48], a thin-film SQUID sensor was used with an integrated multi-turn superconducting coil. A first-order gradiometer was connected to the input superconducting coil, creating a flux transformer. A sample with a 2D electron system was positioned in one of the reception pick-up loops of the gradiometer. The SQUID itself was located in a remote cryostat and was shielded from the stray magnetic field. To reduce noise, measurements were carried out by modulating the gate voltage of the 2D heterostructure, at a frequency of 1.2 kHz, at which the SQUID noise level was the lowest. In the absence of a field, the noise level of the magnetometer was $3.5\times10^{-5}\Phi_0$ Hz$^{-1/2}$ (for $\approx 2\times10^{10}$ electrons in the sample); however, the noise increased with the field, by approximately a factor of 10 already in a field of 6 T.

2.2.2 Modulation technique of magnetic susceptibility measurements. The total orbital magnetization for a typical sample 10^{-2} cm^2 in area with 2.4×10^9 electrons in a field $B = 10$ T amounts to only $\sim 4\times10^{-11}$ CGS. In order to measure such a small quantity, it is necessary to use rather complex electromechanical constructions discussed above, poorly compatible with magnetic field modulation. To solve this technical problem, Fang and Styles [49] modulated the electron concentration, rather than the external magnetic field. Implementation of the much higher frequency reduces the most difficult problem of the low-frequency $1/f$ noise. In experiment [49], the gate voltage of the gated structure was modulated at a frequency of 100 kHz, and to receive the induced signal, a thin-film coil was fabricated on the surface of the insulating Al_2O_3 layer, deposited atop the Al gate.

In order that the picked-up alternating magnetic field not be shielded by the conducting polysilicon gate, the latter was lithographically split into 20 strips, each 25 μm wide. Under harmonic modulation of the gate voltage $V_g = V_{g0} + \Delta V_g \cos(\omega t)$, and, accordingly, modulation of the electron concentration in the 2D layer $\Delta n_s = (1/e)C\Delta V_g \cos(\omega t)$, the voltage $V(t)$ induced in the receiving coil was proportional to the oscillatory component $\mathrm{d}M/\mathrm{d}n_s(B, n_s)$:

$$V(t) = \frac{\mathrm{d}\Phi}{\mathrm{d}t} = \frac{SC}{e}\left|\frac{\mathrm{d}M}{\mathrm{d}n_s}\right|\frac{\mathrm{d}V_g}{\mathrm{d}t} = S\left(N+\frac{1}{2}\right)\frac{\hbar\omega C\Delta V_g}{m^* c}, \quad (4)$$

where Φ is the magnetic flux across the pick-up coil, S is the total area of the 2D channel, C is the capacitance of the gated MOS structure, m^* is the electron effective mass, and N is the Landau level number.

Equation (4) has no fitting parameters; the sample dimensions, area, and capacitance are easily determined. Despite this apparent simplicity, measurement of the absolute amplitude of oscillations with this technique is impeded by the recharging time of the MOS structure, $\sim C/\sigma_{xx} \sim C\rho_{xy}^2/\rho_{xx}$ which for correct amplitude measurements must be much shorter than the modulation period. In practice, this requirement can hardly be fulfilled, especially when approaching the quantum Hall effect, where the conductivity of the 2D system drops exponentially, and therefore the recharging time increases in a 2D structure [50].

2.2.3 Oscillatory magnetization measurements in a system with nonlinear magnetization. In Refs [42, 43], a method was proposed and implemented for measuring the amplitude of electron magnetization oscillations from quantum oscillations of any other quantity (specifically, for example, magnetostriction) under nonlinear conditions of magnetic interaction. The parameter measured in this method is the shape or the spectrum of quantum oscillations; it does not decrease proportionally to the sample volume; this feature, in principle, makes it applicable to systems with a small number of electrons. The method is based on the fact that despite the smallness of the magnetization oscillations δM, i.e., the amplitude of the dHvA effect, the oscillation period for large Fermi surfaces is also small, $\delta B/B \ll 1$, and therefore the differential magnetic susceptibility $|\partial M/\partial B| \sim \delta M/\delta B$ becomes comparable with $1/4\pi$. As the result, the magnetic induction B in the sample differs significantly from the external field, $B = H + 4\pi(1-D)M$ (here, D is the demagnetizing factor).

This difference causes the so-called 'magnetic interaction' or 'Shoenberg effect' [51, 52]. The magnetization M is determined self-consistently by solving the exact nonlinear equation [53]

$$M \sim \sum_{r=1}^{\infty} A_r \sin\left(\frac{\omega r}{H + 4\pi(1-D)M}\right), \qquad (5)$$

where $\omega = cS/(e\hbar)$ is the circular oscillation frequency for the given extremal cross section S of the Fermi surface, and r is the oscillatory harmonic number in the Lifshitz–Kosevich formula [54, 55]. In Ref. [42], Eqn (5) was solved by successive approximations, and the amplitude of magnetization quantum oscillations (orbital electron magnetization) was determined by comparing the spectrum of the measured oscillations with the solution of Eqn (5).

The pioneering experiments in [42, 43, 45, 49] demonstrated the possibility of measuring orbital electron magnetization in nonmagnetic metals and semiconductors; however, in view of the complexity of the methods and their inherent shortcomings, they were little used subsequently.

3. Electron spin susceptibility from charge transport measurements

3.1 Spin susceptibility from monotonic magnetotransport in the in-plane field

To gain information on the spin susceptibility of electron systems from monotonic magnetotransport, measurements are performed (a) in strong fields ($g^*\mu_B B_\parallel \sim E_F \gg k_B T$) or (b) in weak fields ($g^*\mu_B B_\parallel \ll k_B T$).

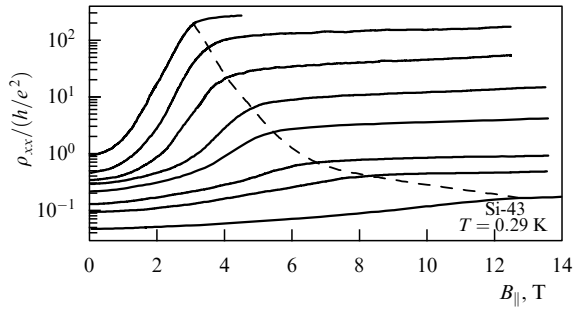

Figure 4. ρ_{xx} as a function of the magnetic field $B_\parallel$ for the 2D system of electrons in silicon at $T = 0.29$ K. Dashed line marks the field of magnetoresistance saturation. Density value (from top down) $n = 1.91$, 1.98, 2.07, 2.16, 2.25, 2.48, 2.70, 3.61 in units of 10^{11}cm^{-2} [59].

3.1.1 High-field measurements. The first method is based on the empirical fact that for the ideal (zero thickness) 2D system, the in-plane magnetic field couples only to the spin degree of freedom. When the magnetic field reaches the complete spin polarization value $B_p = 2E_F/(g^*\mu_B) = (h/e)n/(g^*m^*)$, the magnetoresistance of a 2D system exhibits a feature (in Si-MOS and Si/SiGe, the magnetoresistance $\rho_{xx}(B_\parallel)$ saturates, similarly to what is shown in Fig. 4) [56–63]; from the position of this feature, the renormalized spin susceptibility value $\chi^* \propto g^*m^*$ was determined in a number of papers. Here, g^* and m^* are the renormalized g-factor and the effective electron mass.

The advantage of this method is the simplicity of measurements and apparent simplicity of data interpretation. The disadvantages are connected, first, with the perturbing action of strong fields, which 'cut off' the temperature dependence of χ^* [64]; second, with the field influence on the $g^* = g^*(B)$ value due to the nonlinear character of magnetization [65]; and third, with the disorder effect on the measured magnetoresistance saturation field [59, 66, 67]. Nevertheless, several studies [61] reported the consistency of the χ^* values obtained from the spin polarization field and by other techniques, considered below.

3.1.2 Measurements in low and zero field. Quantum corrections to magnetoconductivity in a weak $B_\parallel$ field originate from the dependence of the effective number of triplet channels of electron–electron interaction on Zeeman splitting. From the magnetoconductivity measured in a weak field $\delta\sigma_{xx}(B_\parallel)$, or from the temperature dependence of the zero-field conductivity $\sigma_{xx}(T)$, we can extract the quantum interaction corrections [64]. According to the theory in [68, 69], their magnitude depends on $g^* = g_b/(1+F_0^\sigma)$ via the Fermi-liquid coupling constant F_0^σ in the e–h triplet channel:

$$\Delta\sigma_{ee}(T, B=0) = \delta\sigma_C(T) + N_t\delta\sigma_t(T, F_0^\sigma). \qquad (6)$$

Here, the first and second terms respectively describe the interaction correction in the singlet and triplet channels, and N_t is the number of triplet channels ($N_t = 15$ for (001)-Si in a weak field and for not too low temperatures [70, 71]).

In the ballistic interaction regime (at 'high' temperatures) $k_B T\tau/\hbar \gg 1$,

$$\delta\sigma_C(T, B=0) \approx \frac{k_B T\tau}{\pi\hbar}\,, \tag{7}$$

$$\delta\sigma_t(T, B=0) \approx \frac{k_B T\tau}{\pi\hbar}\,\frac{F_0^\sigma}{1+F_0^\sigma}\,. \tag{8}$$

For the low-temperature diffusive regime of interaction $k_B T\tau/\hbar \ll 1$, the interaction correction depends logarithmically on temperature [64, 68].

Extracting the quantum correction from transport in a zero field is relatively easy in the ballistic regime using the measured quasilinear T-dependence $\Delta\sigma_{ee}(B=0) \propto T\tau$; as a result of this approach, a number of papers [72–81] reported measurements of the interaction-renormalized g-factor as a function of the carrier density.

For a nonzero $B_\parallel$ magnetic field, and within the same ballistic regime, the interaction quantum correction to magnetoconductivity is

$$\Delta\sigma_{ee}(T, B_\parallel) \approx \Delta\sigma_{ee}(T) + 4\Delta\sigma^Z(E_Z, T, F_0^\sigma)\,, \tag{9}$$

$$\Delta\sigma_{ee}(T, B_\parallel) \propto \frac{1}{\pi}\left(\frac{2F_0^\sigma}{1+F_0^\sigma}\right)\left(\frac{g\mu_B B}{k_B T}\right)^2 \frac{k_B T\tau}{\hbar}\,,$$

where $\Delta\sigma^Z(E_Z, T)$ is a known function of $E_Z \equiv g^*\mu_B B_\parallel$ [69]. We see that $\Delta\sigma_{ee}$ depends quadratically on the field and inversely on the temperature [68–70], which in principle enables us to determine g^*. However, the g^*-factor values determined from magnetotransport in this way typically lead to F_0^σ values not fully consistent with the ones determined from the $\sigma(T, B=0)$ dependence [66, 71, 72]. One reason is the dependence of the theoretical expression for the quantum correction on the character of the disorder potential [68, 69, 82, 83], which for real 2D systems is poorly known [84]. Another reason for the discrepancies is related to the difficulty in disentangling the interaction quantum corrections from classical and semiclassical magnetoresistance effects [85, 86].

In the 'low-temperature' diffusive interaction regime, $k_B T\tau \ll \hbar$, in weak fields $g\mu_B B \ll k_B T$, according to theory [68, 69], quantum corrections to the magnetoconductivity are proportional to $1/T^2$:

$$\Delta\sigma_{xx} \propto \left(\frac{g\mu_B B}{k_B T}\right)^2.$$

Disentangling them from the semiclassical magnetoresistance is a difficult problem [85, 87] (for a more detailed discussion of this issue, see [85, 87, 88]).

The disadvantage of all the transport-type methods of g^*-factor measurements considered in this section is their indirect character; clearly, their results depend on theoretical models, on the simplifying assumptions, etc. An additional complicating factor is the dependence of the spin polarization field on disorder [59, 66, 67]. Finally, all the above methods enable determining only the renormalized g-factor g^*, whereas the effective mass m^* needed to determine $\chi^* \propto g^* m^*$ must be found from other measurements, for example, from the temperature dependence of the quantum oscillation amplitude; the oscillatory methods and effects are discussed below.

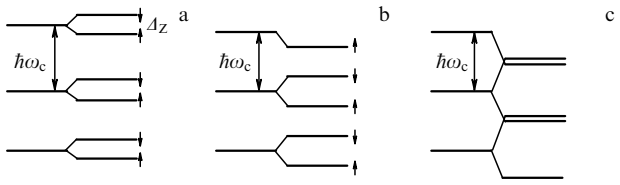

Figure 5. Energy spectrum evolution for a single-valley 2D electron system with a Zeeman splitting Δ_Z: (a) $\Delta_Z \ll \hbar\omega_c$, (b) $\Delta_Z = \hbar\omega_c/2$, and (c) $\Delta_Z \approx \hbar\omega_c$. Vertical arrows depict electron spin polarization.

3.2 Spin susceptibility from quantum oscillations in a tilted magnetic field

The simplest and most widely used method of spin susceptibility measurements for 2D electron systems [89–92] was suggested and first implemented by Fang and Styles [89]. It consists in magnetoresistance oscillation measurements (Shubnikov–de Haas effect, SdH) in a magnetic field tilted from the direction normal to the 2D system plane. The method is based on the fact that the cyclotron energy $\hbar\omega_c$ is related only to the magnetic field component $B_\perp$ perpendicular to the 2D system plane. In turn, the Zeeman splitting of the Landau levels $\Delta_Z = g\mu_B B$ depends on the total magnetic field B_{tot}. In semiconductors, the g-factor value is often close to 2 and the effective cyclotron mass $m^* \ll m_e$ is small; therefore, the Zeeman energy in the purely perpendicular field is usually small compared with the cyclotron gap: $\hbar\omega_c/\Delta_Z = (2/g)(m_e/m^*)(B_\perp/B_{tot})$; this case is schematically shown in Fig. 5a.

As the magnetic field is tilted, the perpendicular field component that enters the orbital effects decreases, whereas Zeeman splitting remains constant. At a certain tilt angle θ, the Zeeman splitting becomes equal to half the cyclotron splitting (Fig. 5b), and the observed oscillation frequency doubles. This condition (so-called 'spin-zero') enables determining the spin susceptibility for the known tilt angle θ as $\chi^*/\chi_b = \cos\theta/0.38$ [90]. Here, $\chi^*/\chi_b = g^* m^*/g_b m_b$, where χ^*, g^*, and m^* are the interaction-renormalized spin susceptibility, the Lande g-factor, and the effective mass; χ_b, $g_b = 2$, and $m_b = 0.19 m_e$ are their band values for (100) Si. This method is applicable for the spectrum shown in Fig. 5a, b and cannot be applied for $\chi^*/\chi_b > 1/0.38 = 2.63$, i.e., for larger Zeeman splitting, as shown in Fig. 5c.

3.3 Spin susceptibility from quantum oscillation interference in the field with a controlled vector

An alternative, more flexible technique for quantum oscillation measurements in a magnetic field with an electrically controlled magnetic field vector was implemented in Ref. [93]. Nowadays, vector magnets are commercially available and are not rare. The magnetic field component $B_\parallel$ in the plane of the 2D system produces an unequal spin subband population, which is needed to determine the spin susceptibility value. The normal magnetic field component is required for observing quantum oscillations related to Landau level quantization and hence for finding the electron population in each spin subband.

As mentioned above in Section 3.2, the conventional way of oscillation measurements in a tilted field [89–91] fails when the Zeeman energy exceeds half the cyclotron energy and further field tilting cannot decrease the Zeeman contribution [94]. The 'crossed-field' measurement technique with independently variable magnetic field components is free of

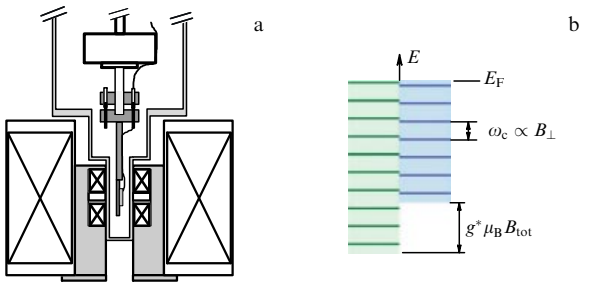

Figure 6. (a) Vector magnetic field setup with two crossed coils. The main superconducting magnet provides the in-plane magnetic field $B_\parallel$ up to 8 T. The second superconducting split coil system, positioned inside the main solenoid, produces the field $B_\perp$ up to 1.5 T normal to the 2D plane. The sample is centered with respect to both solenoids and attached to the cold finger of the mixing chamber ^{3}He/^{4}He [71, 93]. (b) Schematic spectrum of the Landau levels in two spin subbands split by the field B_{tot}.

these limitations and enables expanding the measurement range to low density values n_s, where the Zeeman energy strongly increases due to the spin susceptibility renormalization, as shown in Fig. 5c.

In the presence of a perpendicular field $B_\perp$, the energy spectrum of a 2D system is fully quantized and consists of equidistant Landau levels. Application of the $B_\parallel$ field induces beating of the quantum oscillations, registered as a function of the $B_\perp$ field. The cause of oscillation beating is explained in the right panel of Fig. 6b: the Zeeman splitting of the Landau levels induces nonequal population of the filled Landau levels in the ↑ and ↓ spin subbands. The uppermost Landau levels in the two spin subbands vary with the $B_\perp$ field at different rates. For some $B_\perp$ field values, they cross the Fermi energy E_F in phase and the oscillation amplitudes add constructively. For other $B_\perp$ values, the Landau levels in two subbands cross E_F out of phase, and the oscillation amplitudes are subtracted.

The beat frequency (see Fig. 7) is proportional to the spin polarization of the 2D electron system [94]:

$$P \equiv \frac{n_\uparrow - n_\downarrow}{n} = \frac{\chi^* B_{tot}}{g_b \mu_B}\,, \tag{10}$$

where $n_\uparrow$ and $n_\downarrow$ stand for the populations of the ↑ and ↓ spin subbands, $g_b = 2$ is the bare value of the Lande g-factor for Si, and $B_{tot} = (B_\perp^2 + B_\parallel^2)^{1/2}$. For a degenerate 2D Fermi gas, Eqn (10) can be written in a more convenient way for practical use:

$$P = g^* m^* \frac{B_{tot}}{\nu B_\perp}\,, \tag{11}$$

where $\chi^* \propto g^* m^*$ is the Pauli spin susceptibility of the Fermi liquid, g^* and m^* are the renormalized g-factor and effective mass, and $\nu = nh/(eB_\perp)$ is the Landau level filling factor. We can see that the sought spin polarization and spin susceptibility can be found from the beating period.

Of course, for the interacting system, the shape and amplitude of oscillations may differ from those in the simple Fermi-liquid theory [54, 55, 95, 96], specifically, for the strong inter-electron interaction, for strong overlapping and mixing of the Landau levels, and for the breakup of the Fermi surface into a multiphase state. In particular, for the strong electron–electron interaction case, the semiclassical Lifshitz–Kosevich formula [54, 55] is modified: the interaction effects cause a

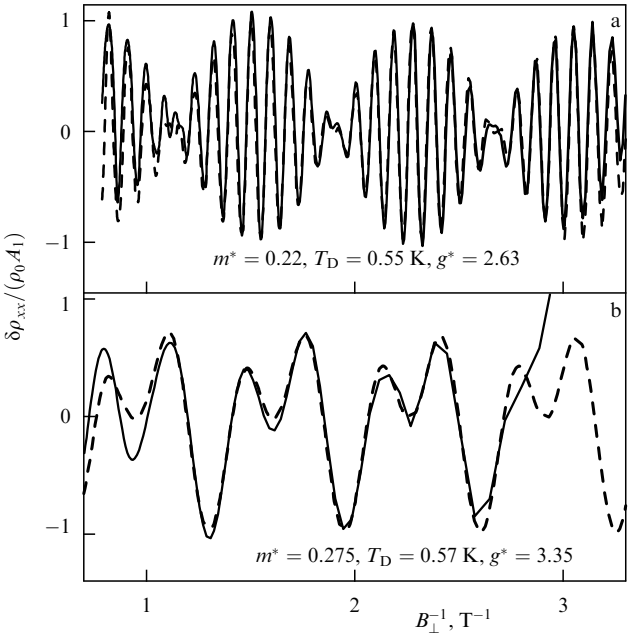

Figure 7. Example of SdH oscillation beating quoted from [97] for (a) $n = 3.76 \times 10^{11}$ cm^{-2}, $T = 0.2$ K, $B_\parallel = 2.15$ T, $P = 20\%$; and (b) $n = 1.815 \times 10^{11}$ cm^{-2}, $T = 0.2$ K, $B_\parallel = 2.5$ T, $P = 64\%$. The data are depicted by solid lines, their approximation using equations [54] (with the parameters shown), by dashed lines. All data are normalized by the amplitude of the first oscillation harmonic $A_1(B)$.

temperature- and magnetic-field-dependent renormalization of m^* and the Dingle temperature T_D [95–97] in the exponential magnetooscillation damping factor.

These complications, however, are insignificant for the beats analysis if the parameters to be determined are only the beating period and oscillation phase, i.e., spin polarization and, eventually, the spin susceptibility. Accordingly, this technique enables the spin susceptibility of *delocalized electrons* with a sufficiently large relaxation time $\omega_c\tau \gg 1$ to be determined.

3.4 Comment

All the techniques considered in Sections 3.1–3.3 for measuring χ^* are based on a comparison of the populations of the two spin subbands, i.e., M/B. This certainly differs from the true thermodynamically defined quantity $\chi_T = \mathrm{d}M/\mathrm{d}B$ considered in Section 4 in what follows. When the same ensemble of electrons contributes to the measured quantity and when M depends linearly on the field, χ^* and χ_T should coincide. Furthermore, the measured susceptibility value is affected by the nonideality of the 2D system, such as the finite thickness of the 2D layer [98–101] and the magnetic field dependence of the susceptibility $\chi(B)$.

4. Thermodynamic methods of measurements

4.1 Capacitive 'floating gate' method for chemical potential measurements

We here consider thermodynamic methods based on measurements of the chemical potential μ and its derivative $\partial\mu/\partial B$; these measurements are probing practically the whole ensemble of charge carriers (including the majority of the localized states) capable of thermalizing within a time

interval of the order of seconds. These methods are based on the Maxwell relation for the second derivatives of the free energy F:

$$\frac{\partial^2 F}{\partial n \partial B} \equiv \frac{\partial \mu}{\partial B} = -\frac{\partial M}{\partial n}\,.$$

A method for measuring the chemical potential variations $\delta\mu$ for a 2D gated system was proposed in Ref. [102]; in fact, it is a version of the Kelvin technique. This method was used to measure $\delta\mu$ as a function of the magnetic field and the electron density in a number of studies [103–106].

4.2 Electrometric measurements of chemical potential variations

The principle of measurements is illustrated in Fig. 8. A 2D electron layer in the MOS structure is located near the Si surface and, together with the metallic gate, forms a parallel-plate capacitor; the gap between the electrodes is filled with silicon dioxide. When a positive potential V_g is applied to the gate relative to the 2D layer (via one of the ohmic contacts with the 2D layer), a charge is induced in the 2D layer, with the magnitude equal to the charge on the gate but of the opposite sign.

If the V_g voltage source is disconnected from the gate, then, at low temperatures, leakage currents are practically absent and the MOS structure keeps the charge $Q = CV_g$ for a sufficiently long time. Hence, the density of electrons in the 2D layer, $n = Q/(eS)$, remains constant (S is the area of the 2D layer and e is the elementary charge); for the same reason, the Fermi energy also remains constant (relative to the lowest size quantization level), $E_F = 2\pi\hbar^2 n/(m^* g_v g_s)$. Here, $g_s = 2$ and $g_v = 2$ are the spin and valley degeneracies on the (100)Si surface [107].

When a magnetic field is applied perpendicular to the 2D plane, the energy of electrons in the 2D system is fully quantized and, in the absence of impurities and electron–electron interaction, the energy spectrum consists of δ-like discrete levels:

$$E = \sum_N \hbar\omega_c \left(N + \frac{1}{2}\right) \pm \Delta_v \pm \Delta_Z\,, \qquad (12)$$

where Δ_v, and Δ_Z are the valley and Zeeman splittings in the spectrum [107], N is the Landau level index, $\omega_c = eB/(m^* c)$ is the cyclotron frequency, and m^* is the electron effective (band) mass in the periodic lattice potential. Accordingly, the Fermi level E_F can have only quantized values. With the Landau level spatial degeneracy $n_H = \Phi/\Phi_0 = eB/(c\hbar)$, the number of filled levels i for a given electron density n is determined by the condition $in_H \leqslant n < (i+1)n_H$ (Φ is the magnetic flux per unit area and Φ_0 is the magnetic flux quantum). When the magnetic field varies, the Fermi level changes in a step-like fashion, jumping from the ith to the $(i+1)$th level. Importantly, the chemical potential changes at a constant electron density n because the gate voltage circuit is disconnected and the recharging current does not flow. Such behavior of the chemical potential is considered conceptually in many textbooks on solid state physics [108–110] and is a prime cause of the quantum oscillations of magnetization (dHvA effect), conductivity (SdH effect), etc.

Variations in $E_F(B)$ are equal to the chemical potential variations, which are detected by the electrometer in the disconnected circuit shown in Fig. 8. In experiments [102],

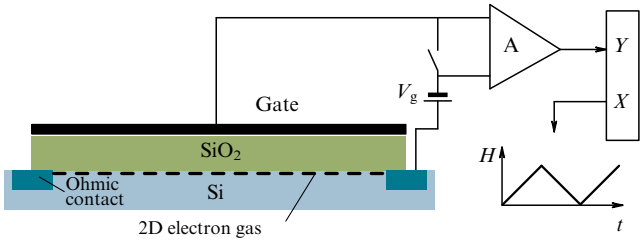

Figure 8. Setup for measurements of chemical potential variations using the 'floating gate' technique [111]. A is the electrometer, X is the variable parameter (magnetic field), Y is the measured signal (chemical potential variation).

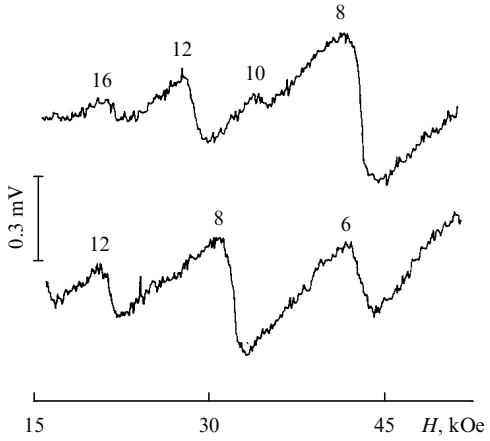

Figure 9. Example of the measured chemical potential variations $\delta\mu(B)$ for the 2D layer of electrons in a silicon MOS structure versus the magnetic field, from Ref. [111]. The electron density is 8×10^{11} cm^{-2}. The line segment on the left shows the magnitude of the effect. The number of filled Landau levels is shown next to each jump of the chemical potential $\mu(B)$.

the magnetic field was swept repeatedly in a sawtooth fashion, whereas the electrometer signal was accumulated coherently with a multichannel analyzer for signal averaging in the time domain.

For accurate electrometric measurements of the potential variations, the gate potential must not change during the measurement time ($t \sim 10^4$ s). This sets rather strict, although feasible, requirements for leakage resistance in the measurement circuit (Fig. 8): $R \gg t/C \sim 10^{13}$ Ω, where $C \approx 1$ nF is the capacitance of the gated structure [111].

To implement the 'floating gate' method, on the studied surface a capacitive structure must be fabricated with a 'reference' electrode, relative to which the chemical potential variations are to be measured. In Refs [111–113], the reference electrode was made of an Al film (gate) deposited on top of the oxide, above the 2D layer. Typical oscillations of the chemical potential in a magnetic field are shown in Fig. 9. The magnetic field derivative of the measured signal, evidently, equals the changes in magnetization per electron $\mathrm{d}\mu/\mathrm{d}B = -\mathrm{d}M/\mathrm{d}n$.

The method described above was also used in Refs [113, 114] to detect chemical potential variations in the gated GaAs/AlGaAs heterostructure, and in Refs [103, 115] to measure fine details of the electron spectrum in the Si-MOS structure. Attempts to measure chemical potential oscillations in bulk crystals of Bi [114] and Be [116] with this

technique were unsuccessful, possibly because of the Fermi level pinning by the bulk carriers in a three-dimensional crystal. For thin YBCO and Ni films, variations in the chemical potential with the magnetic field were successfully detected in Ref. [112].

It is worth noting that this technique enables probing the properties of electrons of the near-surface layer with a thickness of the order of the Fermi wavelength (in the case of a 2D layer of electrons in a quantum well or in an MOS structure) or of the order of the screening length — in bulk samples. A modification of the 'floating gate' technique with measurements of the DC recharging current of the MOS structure was used in Ref. [104] for measurements of the quantum oscillations of the chemical potential as a function of the density of electrons in the 2D layer.

4.3 Modulation capacitive method of measuring chemical potential derivatives

In the early 2000s, the interest of researchers shifted from orbital magnetization to the weaker spin magnetization effects, motivated by the problem of the potential Stoner instability in a strongly correlated 2D electron system. For spin magnetization, a similar modulation method of thermodynamic magnetization (MMTM) measurements was developed in [117], which was subsequently used in Refs [118–120].

The measurement setup for the MMTM method is similar to that shown in Fig. 8. However, to eliminate orbital effects in the spin magnetization measurements, a magnetic field $B_\parallel$ is applied parallel, rather than perpendicular, to the 2D plane. Modulation of the magnetic field $B_\parallel$ at a low frequency ω induces modulation of the chemical potential of the 2D electron layer μ_{2D} and corresponding changes to the equilibrium charge. In contrast to Fig. 8, the recharging current is here measured in the capacitive structure.

The measurement principle is explained in Fig. 10. The MOS structure is equivalent to a parallel-plate capacitor [107]. Due to the overall electroneutrality of the sample, the electron layer charge is exactly equal (with an opposite sign) to the charge on the gate electrode. When a DC voltage V is applied to the gate, the free energy of the system becomes

$$F = F_g + F_{2D} - enV + \frac{e^2 n^2}{2C_0}\,, \tag{13}$$

where F_g, and F_{2D} are the free energies of the Al-gate film and the 2D layer. The typical oxide thicknessis $d_{ox} \approx 200$ nm, whereas the effective 'distance' of the 2D layer from the interface Si/SiO_2 is $z_0 \approx 3.5$ nm and remains almost constant; therefore, the capacitance C_0 in Eqn (13) differs only a little from the geometric capacitance of the classic capacitor, by $\sim (z_0/d_{ox}) \sim 1.7\%$:

$$\frac{e^2}{C_0}\frac{dn}{dB} = -\frac{\partial\mu_{2D}}{\partial B} + \frac{e^2 n}{C_0^2}\frac{\partial C_0}{\partial B} \approx -\frac{\partial\mu}{\partial B}\,. \tag{14}$$

The capacitor recharging current δI equals [117, 120, 121]

$$\delta I = \frac{i\omega C_0 \delta B}{e}\frac{\partial\mu}{\partial B}\,, \tag{15}$$

where δB is the amplitude of the magnetic field nodulation and C_0 is the capacitance of the 'gate–2D layer' capacitor, measured independently by a conventional capacitance bridge. Contributions to the measured capacitance due to electron–electron interactions and the finite width of the 2D layer are negligibly small [120, 121].

The quantity $\partial\mu/\partial B$ is found from the measured recharging current and, due to the Maxwell relation $\partial M/\partial n = -\partial\mu/\partial B$, directly yields the sought 'magnetization per electron' $\partial M/\partial n$, which can then be integrated with respect to n to obtain the absolute value of the magnetization $M(B, n)$. The magnetic susceptibility χ is calculated from the slope $M(B, n)$ as a function of B in low fields. A DC field applied parallel to the modulation field enables determining the nonlinear magnetic field dependence of $\partial M/\partial n$ and $M(n)$.

Importantly, all electrons capable of thermalizing during the field modulation period (in the 0.1–1 s range) contribute to the magnetization measured by this method [120, 121].[1] This difference in characteristic times (ps in transport measurements and seconds in thermodynamic measurements) sets a fundamental difference in the character of information obtained from measurements with two different techniques. In oscillatory transport measurements, only delocalized (mobile) electrons participate, but in thermodynamic measurements practically all electrons, delocalized and localized, contribute. This enables carrying out thermodynamic measurements even in the insulator state, where the sample resistivity rises to the giga-ohm range.

In Ref. [121], the applicability of this method was also justified for measurements in the regime of complex capacitance, which acquires an imaginary part due to contact and

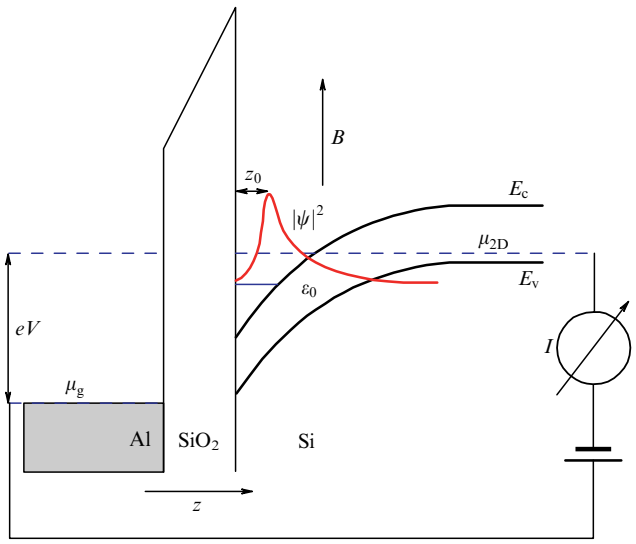

Figure 10. Energy diagram and the principle of modulation-type measurements of spin magnetization in a magnetic field parallel to the 2D plane [117, 121]. V is the voltage applied to the gate of the MOS structure; μ_{2D}, and μ_g are the chemical potentials of the 2D layer and the gate, and E_c and E_v are respectively the bottom of the conduction band and the ceiling of the valence band in bulk Si; I is the current amplifier of the fA range.

[1] The SiO_2/Si interface is a disordered intermediate SiO_x layer, a few atomic layers thick, where the broken bonds are saturated with hydrogen in the process of Si-MOS structure fabrication [107, 122]. The localized states formed at the interface contribute to the threshold voltage V_t in the relation between the density of mobile carriers n and the voltage V_g applied at the gate of the MOS structure $n = (C/e)(V_g - V_t)$. For the studied high-mobility Si-MOS structures, the density of these localized interface states is 10^{10} cm^{-2}; at low temperatures, they do not recharge for many years, making electrometric measurements of the chemical potential possible. The neutral interface dipoles contribute to potential fluctuations in the 2D layer and to shallow electron localized states. The latter do not participate in charge transport; however, they thermalize and recharge over millisecond times.

channel resistances; the latter enable the range of applicability of the thermodynamic method to be expanded deep into the low-density regime of the insulator state.

Using the MMTM, in Refs [117, 118] magnetization per electron dM/dn was measured in a strong magnetic field for the 2D electron system in Si. As a result, anticipated features of magnetization at the full spin polarization field were revealed. Besides the 2D electron system in Si, thermodynamic properties of electrons were measured in GaAs heterostructures [123, 124] and in HgTe quantum wells [125] using this method. The main physical results of these measurements are reviewed in Section 6.2.2 below.

5. Methods of local spin magnetization measurements

The need for local methods of magnetic measurements emerged in relation to the discovery of a class of similar spin–orbit effects: the spin Hall effect (SHE), the inverse spin Hall effect (ISHE), the quantized spin Hall effect (QSHE), spin currents, etc. Studies in these fields are related to the development of spintronics, in particular, semiconductor spin logic elements, electric and optical means of spin magnetization control [126–128], and, more generally, the need for effective information storage and computing devices.

The spin Hall effect reveals itself in the accumulation of spin polarization at sample boundaries when electric current flows in the bulk; importantly, oppositely directed spins are accumulated at the opposite edges of the sample. The idea of the spin Hall effect goes back to the anomalous Hall effect (AHE), which was already observed by E Hall in ferromagnetic materials. In the absence of ferromagnetism, the spin–orbit interaction (SOI), which is a relativistic effect, also leads to effects of spin accumulation, e.g., due to the asymmetry of carrier deflection in scattering processes [128, 129]. In the ordinary Hall effect, the Lorenz force deflects the charged carriers toward the sample edges, thus producing an electric field directed perpendicular to the current. By contrast, in the anomalous Hall effect, the SOI produces the force deflecting carriers to the opposite sample edges depending on the spin direction.

The relation between the charge and spin currents in nonferromagnetic materials due to SOI was theoretically predicted in 1971 by Dyakonov and Perel [130, 131]. The idea of an experiment was suggested in Ref. [132], and the first measurements were done in [133, 134]. This so-called 'extrinsic' SHE is related to an asymmetry of electron scattering in the presence of SOI and is an analogue of Mott scattering and the deflection of an electron beam in a vacuum; its principle is schematically explained in Fig. 11. The process of charge carrier scattering by impurities includes a spin-dependent difference in the deflection probability, which causes an imbalance between oppositely directed spins.

The 'extrinsic' SHE was subsequently supplemented with the predicted [135, 136] strong 'intrinsic' SHE [137–139], related to dissipationless spin currents and irrelevant to electron scattering; its physical mechanism is illustrated in Fig. 12. The inverse SHE (ISHE), discovered in 2006 [140–142], enables electric sensing of the spin current or the spin magnetization gradient. For experiments with the SHE, materials are selected with high spin–orbit coupling parameters, such as GaAs ($\lambda_{SO} = 5$ Å^2) or ZnSe ($\lambda_{SO} = 1$ Å^2).

Several reviews have already been published in this booming field, including [127, 143]; thanks to them, we

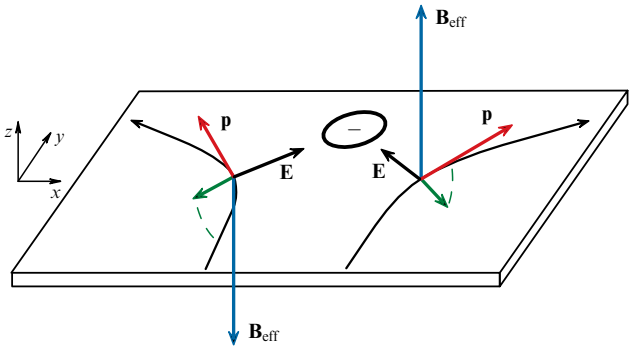

Figure 11. (Color online.) Generation of the extrinsic SHE in a system with SOI. Electrons move in the xy plane in a system with broken inversion symmetry $z \to -z$ and are scattered by a negatively charged center. Red arrows show momentum direction, green arrows show the equilibrium direction of spins in a system with a Rashba-type spectrum. In the vicinity of the charged center, electrons are deflected by an electric field $\mathbf{E}$. In this process, the electron experiences an effective magnetic field $\mathbf{B}_{\text{eff}} \propto [\mathbf{p} \times \mathbf{E}]$ (blue arrows), which is perpendicular to the xy plane, and is inhomogeneous due to the momentum dependence. The gradient of the Zeeman energy (of this effective field) forces spin rotation and their exit out of the xy plane, as shown by the dashed arcs. The effective magnetic field is directed oppositely for electrons scattered to the left and right, thus leading to accumulation of spin magnetization in opposite directions at the sample edges.

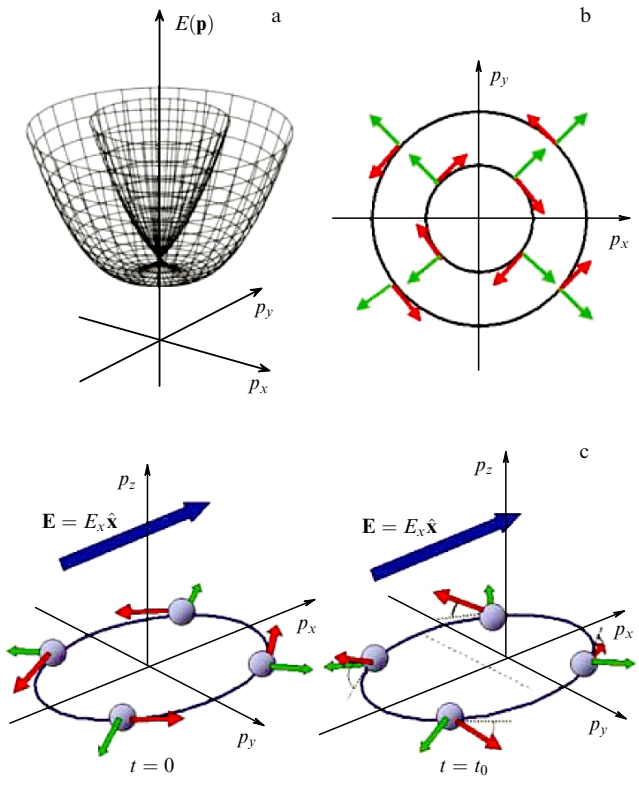

Figure 12. (Color online.) (a) Energy spectrum of electrons with a Rashba-type Hamiltonian for a 2D system with SOI, and (b) the spectrum projection on the xy plane (Fermi surface, FS). Radially directed momenta are marked with green arrows on the FS, and the spin eigenvalues, with red arrows. (c) Under application of an electric field in the x direction, the FS shifts by $|eE_x t_0/\hbar|$ over a time $t_0 < \tau$ (where τ is the characteristic scattering time). When an electron moves in momentum space in the presence of an electric field E_x, the effective torque brings the spins out of plane: upward for $p_y > 0$ and downward for $p_y < 0$, thus causing the spin current in the y direction. (From Ref. [137].)

avoid describing the field in detail, and only briefly discuss the physical essence of the effects, experimental techniques, and the most remarkable results.

5.1 Detecting local spin polarization

5.1.1 Detection using optical techniques. Problems with SHE detection were initially due to a lack of measurable electric signals; for this reason, the first experiments were done by optical methods [144–146]. In experiments, Kerr rotation of polarization was detected (with spatial resolution) for light transmitted through the epitaxial layers of p–GaAs, n–InGaAs [144], n–GaAs [147, 148], n–ZnSe [146], and InGaN/GaN [149] superlattices, etc. The polarization rotation indicates electron spin accumulation at the sample edges, perpendicular to the applied electric field. The typical geometry of measurements is shown in Fig. 13. A beam linearly polarized along z was directed normally to the plane of a rectangular sample and focused onto a spot about 1 μm in diameter. The parameter to be analyzed was the polarization rotation angle of the reflected beam; it is proportional to the spin magnetization in the z direction. Such a setup allows detecting an angle-resolved photoluminescence signal at the opposite edges of the 2D hole system. For precise sample positioning relative to the incident beam, a precise piezo-drive was used in Ref. [148] with a 1 μm coordinate resolution. In all measurements [144–146, 148], a Ti:sapphire laser with mode locking was used, with a typical 0.15–1 ps pulse duration and 76 MHz repetition rate; the wavelength of 825 nm was tuned to the semiconductor absorption edge. In some experiments [146], a pump-probe technique was used.

Results of the Kerr rotation measurements are shown in Fig. 13. The rotation angle corresponds to the z component of spin polarization, which diminishes with the applied in-plane external magnetic field because of spin precession. The maximum Kerr angle is reached when the external field $B_{\rm ext}$ equals the intrinsic spin magnetization, $B_{\rm int}$; this qualitative consideration helps to estimate the spin magnetization at the edges. By taking similar measurements with a uniaxially strained InGaAs sample and observing no Kerr rotation anisotropy, the authors concluded that the observed effect in all cases was the 'extrinsic' rather than 'intrinsic' SHE. Analogous measurements were performed in [150] in the Voigt geometry with a beam transmitted through the strained epitaxial layers of InGaAs and GaAs. In all cases, the authors observed a similar magnitude of the rotation angle: ~ 4 μrad for $E = 4$ mV μm^{-1}.

The above experiments were performed in the regime of a 'weak' spin-orbit coupling, i.e., when the spin–orbit splitting is smaller than the disorder-induced level broadening. In the 'strong' SOI regime, measurements were taken in [145], where the studied 2D hole layer was part of a p–n junction in a light-emitting diode. The current flowing through the p–n junction is accompanied by electroluminescence due to electron–hole recombination. Beyond the ordinary exciton luminescence, the electroluminescence spectrum contained a circularly polarized broadened line. Because of the optical selection rules, the circular polarization in a certain direction points to spin polarization in this direction of carriers involved in the recombination.

In all experiments, the Kerr angle $\theta_{\rm el}$ (or the spin accumulation magnitude n_0), in accordance with the theory, was found to be linear in the electric field E. The spin relaxation time τ extracted from data approximation (e.g., in

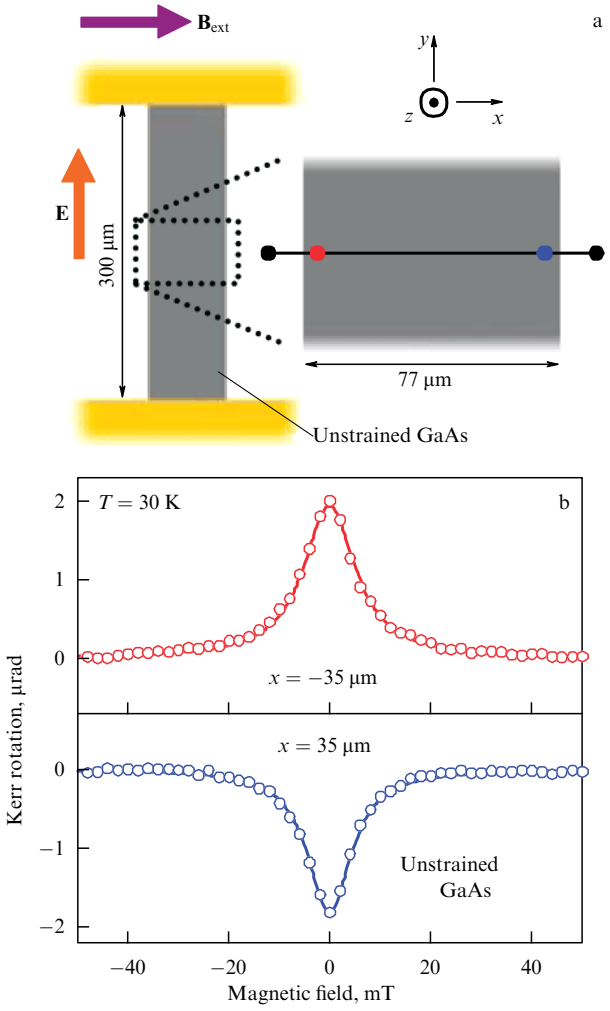

Figure 13. (Color online.) Spin Hall effect in unstrained GaAs, from Ref. [144]. (a) Sample geometry. (b) Typical measurement of the Kerr rotation versus magnetic field $B_{\rm ext}$ at two sample edges, $x = \pm 35$ μm, for $E = 10$ mV μm^{-1}.

Fig. 13), was fit to a Lorentzian $\theta_{\rm el} = \theta_0/[1 + (\omega_{\rm L}\tau)^2]$; it did not depend on E, but was coordinate dependent, increasing with the distance from the edges. At 20 K, the peak value of the spin density near the edges was estimated as $n_0 \sim 16$ μm^{-3}. Assuming a simple spin diffusion model, we can assume the spin accumulation profile related to the spin current to be $\theta_{\rm el} = n_0 \,\mathrm{sech}\,(W/2L_{\rm s}) \sinh\,(y/L_{\rm s})$, where $L_{\rm s}$ is the spin diffusion length. From the approximation of experimental data in Ref. [146], an estimate $L_{\rm s} \approx 1.9$ μm was found for $T = 20$ K. The spin current density along y can be written as $|J_y^{\rm s}| = L_{\rm s} n_0/\tau$, whence the spin conductivity is $\sigma_{\rm SH} = -J_y^{\rm s}/E_x \sim 3\ (\Omega\,\mathrm{m})^{-1}/|e|$.

It is important to note for potential applications that as the temperature increased, the magnitude of the effect diminished (as did the spin polarization n_0, the spin relaxation time τ, and the spin diffusion length, the last from 1.9 μm at 20 K to 1.2 μm at 295 K), but the effect remained pronounced even at room temperature.

5.1.2 Detection using electrical methods. For electrical detection, setups with a nonlocal geometry are used, in which spin-polarized carriers are injected from a ferromagnetic to a nonmagnetic material. The detection method is commonly

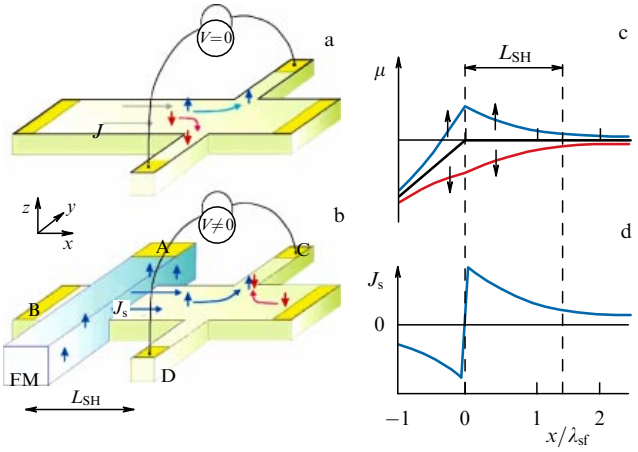

Figure 14. (Color online.) (a) Direct SHE: the spin imbalance arises at the sample edges due to SOI when purely charge current flows. (b) ISHE: the Hall effect, induced by the spin current. A purely spin current J_s is injected from left to right. SOI causes separation of electrons with spins up and down, thereby inducing the transverse charge current and noticeable voltage. Schematic coordinate dependences (c) of electrochemical potentials for spins ↑ and ↓, when the charge current flows from the ferromagnet to a nonmagnetic material from left to right, and (d) of the spin current J_s related to spin injection. Reproduced from Ref. [152].

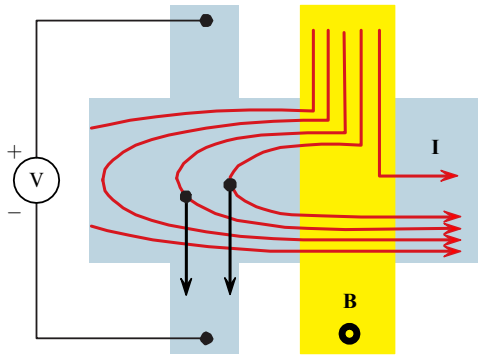

Figure 15. (Color online.) Current distribution in the vicinity of a ferromagnetic contact [143].

based on the ISHE, where the Hall voltage is induced by spin current. Many experimental setups are described in the literature [140, 143, 151–156]; they use various nonmagnetic materials, including normal metals, superconductors, and nanotubes.

Two different approaches are mainly used for the nonlocal electric detection of SHE: (1) detecting the 'direct SHE', i.e., spin accumulation at two edges of a sample due to SOI, under the flow of a charge current of unpolarized carriers and detecting the spin magnetization accumulated at the edges with ferromagnetic potential contacts [143, 155, 157], and (2) detecting the 'inverse SHE' (ISHE) by injecting polarized charge carriers via ferromagnetic current contacts and by detecting imbalance in spin accumulation at the edges with nonmagnetic potential contacts [154, 158–160].

Schematic setups of nonlocal electric detection by the second method (ISHE) are shown in Fig. 14. If the charge current is spin unpolarized (Fig. 14a), it generates spin accumulation at the sample edges (as it does in the SHE), not leading to the appearance of a Hall voltage because equal numbers of charge carriers deflect to opposite sides. However, if the charge current is spin polarized (Fig. 14b) by means of ferromagnetic injection with the magnetization directed out of plane, the initial imbalance of electrons with spins ↑ and ↓ causes an inequality of electrons scattered to different sides. As a result, a Hall voltage arises between the Hall contacts C and D. The Hall voltage is measured nonlocally, away from the injector, whereas the Hall contacts and injector are disconnected galvanically in order to avoid voltages generated by the ordinary Hall effect and by magnetoresistance anisotropy. Therefore, the Hall effect induced by the spin current shown in Fig. 14b is the inverse effect of the SHE shown in Fig. 14a.

The polarized electrons are injected in the vicinity of $x = 0$ and diffuse with equal probabilities toward two opposite arms of nonmagnetic material. The process of nonlocal current flow is illustrated in Fig. 15. In the diffusion process, the nonlocal spin current J_s decays with the distance from the injection point as [152]

$$J_s(x) = \frac{P}{2}\left(\frac{I}{A_N}\right)\exp\left(-\frac{x}{\lambda_{sf}}\right), \tag{16}$$

where P is the polarization of the injected current $I = I_{AB}$ (Fig. 14b), A_N is the cross-sectional area of the nonmagnetic strip, and λ_{sf} is the spin diffusion length. For the geometry shown in Fig. 14b,

$$V_{SH} = V_{CD} = -\frac{E_y(x)}{w_N} = w_N\frac{\sigma_{SH}}{\sigma_c^2}J_s(x), \tag{17}$$

where w_N is the width of the nonmagnetic metal strip, σ_c is the Drude conductivity for the charge current, and σ_{SH} is the 'spin-Hall' conductivity. Substituting Eqn (16) in Eqn (17), we obtain the nonlocal Hall resistance $R_{SH} = R_{AB,CD} = V_{SH}/I$:

$$R_{SH} = \frac{P}{2t_N}\frac{\sigma_{SH}}{\sigma_c^2}\exp\left(-\frac{x}{\lambda_{sf}}\right).$$

In practical devices [151], CoFe was chosen as the ferromagnetic material, and Al as a normal metal. The tunnel barrier between Al and CoFe is achieved by oxidation of the Al strip. The presence of the tunnel barrier is essential for uniform distribution of the injected current, as well as for increasing the polarization of injected electrons. Typical parameters of this device are $P \approx 0.28$, and $\lambda_{sf} \sim 450$ and 700 nm for the respective Al strip thicknesses of 12 and 25 nm. The spin diffusion length sets the required strip length $L \sim 500 - 800$ nm.

An elegant setup for nonlocal ISHE detection in a double-arm H-bridge was realized in Ref. [156]. Usually, to detect the ISHE with two-arm bridges, spin-polarized carriers are injected via a ferromagnetic contact [160]. Unlike this, for spin polarized current injection in Ref. [156], an HgTe/CdHgTe heterostructure was used with an HgTe quantum well whose thickness was greater than 6.3 nm. Due to the spectrum inversion, the regime of a topological insulator sets in this structure, with the spin-polarized current flowing along the edges, which allows relinquishing ferromagnetic contacts.

The idea of ISHE detection using the double H-bridge was suggested in Ref. [161]. Such a setup was used to measure the SHE in Au films [162], PbTe layers [163], and graphene [164]. The principle of its operation is explained in the inset to Fig. 16. A current of unpolarized charges J_y flows in the middle arm B. In the presence of SOI, the dominant scattering direction depends on spin; as a result, a spin current

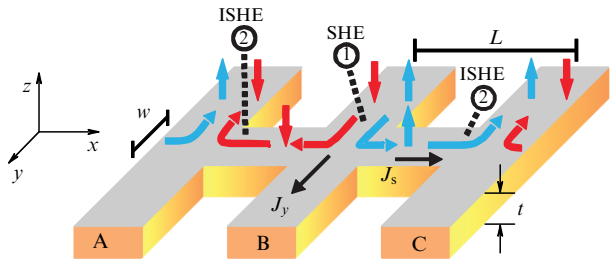

Figure 16. (Color online.) Configuration of measurements with a double H-bridge, from Ref. [143].

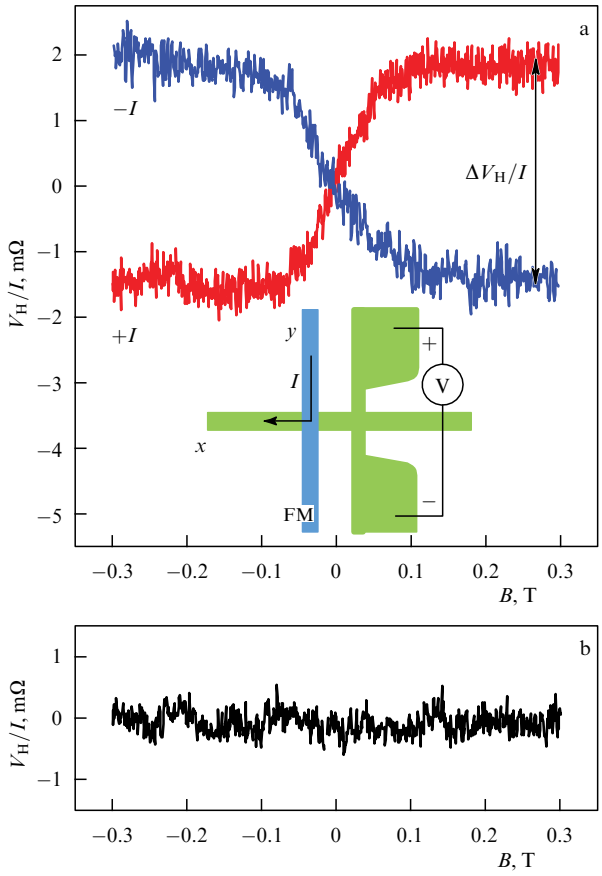

Figure 17. (Color online.) (a) ISHE signal versus the external field B applied along x for a device with an InAs channel $L = 2.83$ μm long at $T = 1.8$ K. FM — ferromagnetic injector strip. Red curve: current $I > 0$, blue curve: $I < 0$. The inset shows the geometry of measurements. (b) Control measurement with B applied along the y axis, demonstrating the absence of the Hall voltage. Inset: geometry of measurements (Ref. [160]).

J_s arises in the perpendicular direction. Due to the ISHE, carrier scattering induces a charge current in the y direction, perpendicular to the current J_s (ISHE), and a difference between potentials (or a current) is induced in arms A and C. Despite the doubtless advantage of the double H-bridge, due to the absence of ferromagnetic contacts the interpretation of results is hampered by the presence of side effects related to overheating of arm B (due to the Nernst–Ettingshausen effect) and diffusive transport [143].

The majority of the devices utilize the extrinsic SHE caused by scattering anisotropy in the diffusive transport regime. The ballistic regime of the intrinsic SHE [156, 160] was realized only for materials with a large carrier mean free path at low temperatures (e.g., InAs) and for devices with a short channel. In Ref. [160], the method was used to detect spin precession under the ballistic propagation of carriers injected from a ferromagnetic contact (Fig. 17) into the perpendicular strip of a nonmagnetic material with a large SO coupling (InAs quantum well).

When carriers are injected from a contact polarized by an external field B along the x direction and are accelerated by an electric field to the left side into the $x < 0$ region, then, in the nonlocal ballistic regime, the charge current is zero in the region $x > 0$ (see Fig. 15). In materials with a Rashba spectrum, the spins tend to align perpendicular to the electron velocity v_x and to the built-in electric field E_z of the quantum well. In this picture, the spin directed initially (at $x = 0$) along x starts precessing as a function of x. Heuristically, we can imagine that both the electron trajectory and the Hall voltage $V_y \equiv V_H$ between the strip edges exhibit spatial oscillations [165] with a period $\lambda = \pi\hbar^2/(\alpha m^*)$, where α is the Rashba spectrum parameter. As a result, the Hall voltage shows antinodes at distances $x = \lambda/4$, $3\lambda/4$, etc. Its sign inversion under current inversion is seen in Fig. 17a. For the magnetization directed along y, the carriers injected into InAs propagate ballistically with no spin precession or trajectory bending, and the Hall voltage does not arise (Fig. 17b).

Numerous experiments confirmed the operational capability of the described devices and the ability to electrically detect the SHE. Quantitative data regarding the parameters of spin diffusion, the spin diffusion length λ_{sf} and its temperature dependence, were obtained [143, 152].

5.2 Magnetometry based on NV centers

The methods described in Section 5.1 allow sensing electron spin magnetization with a spatial resolution of the order of 1 μm. However, in some cases there is a need to study magnetization features on a nanoscale. In magnetic materials and nontrivial magnetic phases, such as skyrmions, magnetic topological insulators, spin density waves, and Abrikosov vortices in superconductors, nonuniform magnetic structures arise on the nanoscale. Negatively charged nitrogen-substituted vacancies (NV centers) in diamond offer the possibility of sensing on the atomic scale, suitable for quantum magnetization probing with nm resolution.

Figure 18a shows an NV center in the diamond lattice, and Fig. 18b displays schematic energy levels. The NV center

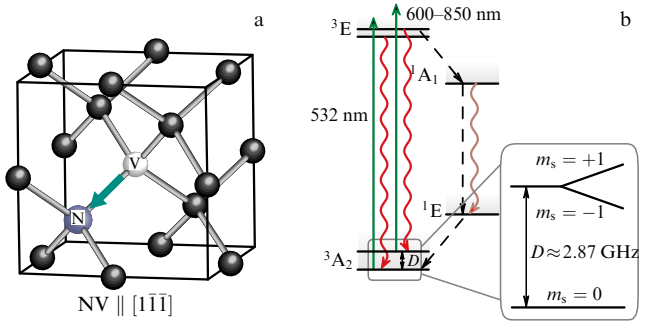

Figure 18. (Color online.) (a) Diamond lattice containing an NV center formed by the substituent nitrogen atom neighboring the carbon vacancy in the lattice. The green arrow shows the symmetry axis of the NV center along the [111] direction of the diamond lattice [171]. (b) Energy diagram of an NV center in diamond containing zero-field split electron levels with the spin projection $m_s = 0$ and degenerate levels with $m_s = \pm 1$ (Refs [172, 173]).

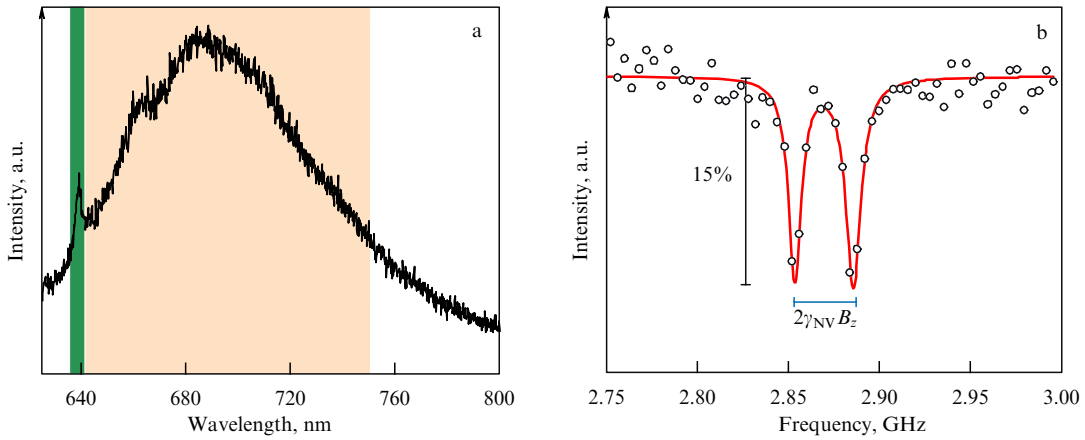

Figure 19. (Color online.) (a) Typical luminescence spectrum with a narrow ZPL and wide PSB. (b) Example of results of ODMR shows two dips in the luminescence intensity, located symmetrically relative to the zero field splitting of 2.87 GCs Ref. [169].

in diamond consists of a substituent nitrogen atom neighboring the carbon vacancy. Such centers emerge in bulk and nanocrystalline diamonds — synthetic diamonds grown by CVD, as a result of radiation damage and annealing, or by ion implantation and annealing. The centers exist as negative (NV^-) and neutral (NV^0) charge states [166]. Besides diamond, vacancy centers have also been found in silicon carbide (SiC) [167, 168].

Schematics of the NV^- center and energy level structure are shown in Fig. 18. The ground (^3A) and excited (^3E) states form a triplet with sublevels $m_s = 0$ and $m_s = \pm 1$. The transition $^3A_2 \rightarrow {}^3E$ can be excited in the optical wavelength range 450–637 nm, and the fluorescence of the transition $^3E \rightarrow {}^3A_2$ occurs in the wavelength range 637–800 nm.

Figure 19a shows a luminescence spectrum at room temperature [169]. The purely electronic transitions between the excited ^3E and the ground ^3A states lead to a narrow zero-pnonon line (ZPL) at 638 nm. Beside this line, there is a wide phonon side band (PSB), shifted to the red side; it contains about 96% of the intensity of the NV-center luminescence [170].

Optical transitions mainly occur with spin conservation; however, the spectrum contains level crossings between the singlet and triplet states. Therefore, beside the direct transition from ^3E to ^3A, the fluorescence decay channel also includes intermediate long-lived singlet states, as well as radiationless transitions from ^3E to $^1A_1$ and from ^1E to $^3A_2$. As a result, the relaxation rate to the $m_s = 1$ state is higher than to the $m_s = 0$ state. Because of this difference, under optical pumping, an optical spin polarization develops: a major part of the population transfers to the $m_s = 0$ state. The fluorescence of the NV center is spin dependent and its level is determined by the spin polarization degree. Such dynamics of the level population allow polarizing the electron spin of the NV center via a nonresonant excitation (typically at the 532 nm wavelength, by 1 μs pulses).

In the NV^- center, the singlet and triplet spin sublevels $m_s = 0$ and $m_s = \pm 1$ of the $^3A_2$ ground state in a zero field are split by the crystal field: the energy difference is $D = 2.87$ GHz (Fig. 18). A weak external magnetic field shifts the sublevels $m_s = \pm 1$ such that their splitting varies proportionally to the field projection B on the NV-center axis: $[1/(hB)][E(m_s = \pm 1) - E(m_s = 0)] = 2.8$ MHz G^{-1}. Therefore, the NV^- centers can be detected not only in the optical transition between the ground $^3A_2$ and excited ^3E levels but also in the microwave (MW) range, using conventional electronic paramagnetic resonance (at a frequency of 2.87 GHz in a zero field) or by optically detected magnetic resonance (ODMR) [174–176]. In the latter case, the applied resonant microwave radiation transfers part of the population from $m_s = 0$, decreasing the fluorescence signal excited by nonresonant optical pumping. The properties of NV centers are reviewed in detail in Ref. [166].

Figure 19 shows an example of optical detection — optically detected magnetic resonance (ODMR), which is a sharp intensity drop of the narrow luminescence line under coincidence of the microwave signal frequency with spin sublevel splitting. The unique distinction between NV centers and other solid-state systems with single spins is that a long coherence time is achieved, even at room temperature. Thanks to this feature, an individual NV center in diamond crystal with a low defect density can provide a threshold sensitivity as low as 30 nT Hz$^{-1/2}$ [174] and even 4.3 nT Hz$^{-1/2}$ [177] at room temperature and in the atmospheric environment.

The second unique feature of NV centers is the small volume of the sensor, practically on an atomic scale. This enables bringing the sensor to a sample at a nanometer-distance for visualizing the magnetic field on the nanoscale. The magnetic field of individual spins decays as the third power of distance and, were a sensor located ~ 1 mm away, the field from a single spin would be negligibly low, $\sim 10^{-21}$ T. However, NV centers can form within 5 nm of a diamond surface, at the same time preserving a long enough spin relaxation time, 100 μs [178]. The proximity of an NV center to the diamond surface enables sensing the magnetic field of individual spins in the range of μT [174, 177, 179–181].

Scanning microscopy based on NV centers. Magnetic sensors with NV centers are compatible with the scanning probe microscopy technique; owing to this circumstance, they are used for visualizing magnetic fields on nanoscales. In the scanning magnetic NV microscope, the diamond nanopillar serves not only as the probe tip but also as a nanophotonic light guide. In the latter capacity, it effectively collects and guides a photoluminescence signal from the NV center to the optical registration system [182]. A schematic arrangement of an NV magnetometer with optical sensing is shown in Fig. 20. The theory of magnetic scanning NV-magnetometer operation and means of their optimization are considered in [169, 173].

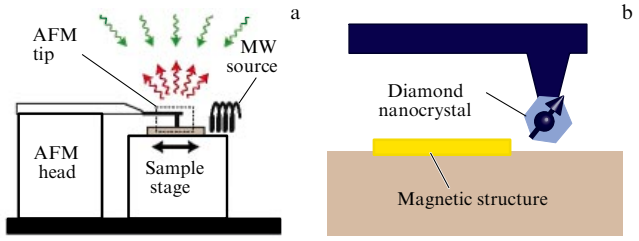

Figure 20. (Color online.) (a) Diagram of an NV magnetometer [179]. (b) Setup of an atomic force microscope (AFM) with a diamond nanocrystal probe containing a single NV center [183].

In this relatively young area, several reviews and monographs have already been published [166, 169, 173, 183–188], as have PhD dissertations [189].

Various applications of NV magnetometry for studying ferromagnetic 50 nm grains in magnetostatic bacteria, 10 nm grains in meteorites, and magneto-marked cancer cells have been described [190–192]. Owing to the high spatial resolution and nontoxicity of diamond, NV microscopes are successfully used in neuroscience and biology [184], including detecting the intracellular dynamics of a living cell [193, 194]. NV magnetometers are expected to enable imaging of individual molecules by NMR and MRI techniques; detecting a single electron spin was already demonstrated [195].

Traditional technological applications of NV magnetometers are the characterization of read/write magnetic heads, measurements of stray fields from magnetic domains in hard disk drives, etc. [179, 196]. In condensed-matter physics, NV magnetometry was used to study the Meissner effect, the structure of magnetic flux vortices in superconductors [197], the structure of domain walls and vortices in thin magnetic films [198, 199], spin-wave excitations [200], skyrmions, spin ice, and other exotic materials [182, 201].

5.3 Scanning probe magnetometers

Besides the magnetic microscopy based on NV centers considered in Sections 5.1 and 5.2, more traditional methods are also widely used for local magnetic surface probing.

5.3.1 Scanning magnetic force microscopes. Since the first realization of the magnetic force microscope in 1987 [202], a great number of magnetic force microscope (MFM) designs have been developed and described in detail in the literature [202–204]. To date, they have become common in laboratory practice and are commercially available as an option for atomic force microscopes (AFMs) [205].

The probes typically used for measurements with MFMs are made either of magnetic materials or with a magnetic film (Co) deposited onto an ordinary nonmagnetic probe [206]. In the latter case, the stray magnetic fields in the vicinity of the tip are smaller by an order of magnitude than for probes made of magnetic wires. In MFM measurements in the static regime, the probe — the magnetic tip — must be located away from the surface, in order that the magnetic interaction forces exceed the Van der Waals forces (the dominant forces in the AFM regime). Because of this, MFMs have a limited spatial resolution. MFM measurements usually require two cycles of scanning: at a short distance to the surface and at a long distance, with subsequent subtraction of the results to eliminate contributions from Van der Waals interactions.

Bimodal MFM designs have also been developed; they enable measuring AFM and MFM signals in a single scan. For this purpose, small-amplitude (~ 10 nm) mechanical oscillations are excited in the elastic console simultaneously at two frequencies; by lock-in detecting AC signals at two frequencies, the contributions from the long-range magnetic forces (MFMs) and from short-range Van der Waals forces (AFMs) [207–211] are disentangled.

5.3.2 Magneto-resonant force microscopy. This method (MRFM) combines ESR and NMR methods with MFM [212, 213] and, in principle, allows the 3-dimensional imaging of magnetization inside materials; several reviews on MRFM have been published, e.g., [203, 214]. Like MFM, MRFM uses an elastic console with a probe at its end, located at a short distance to the sample. A microwave field with the frequency tuned to the magnetic resonance changes the spin orientation (of electrons or the nuclei) and hence the sample magnetization. This causes a change to the magnetic force acting on the sample and shaking of the elastic console. To improve the MRFM sensitivity, the amplitude of the microwave field is modulated at the frequency of the console mechanical resonance; thereby, the amplitude of its forced vibrations becomes the measure of the sought magnetization.

When the probe is scanned relative to the sample, the resonant vibration amplitude (of the angstrom scale) of the cantilever holding the sample is measured. This method is applicable for magnetic mapping with the pumping of either electron spins at the ESR frequency or nuclear spins at the NMR frequency. In earlier studies [215], a spatial resolution of ~ 5 μm was obtained. Subsequently, the spatial resolution was improved to 0.9 nm [216], whereas the sensitivity reached $50-100\,\mu_B$ nuclear magnetons (for a $3-5$ nm^3 voxel) [217]. Such magnetometers are now also commercially available [218].

5.3.3 Scanning Hall microprobes. Scanning Hall magnetometers have a rather simple design and can operate in a wide temperature range and in the atmospheric environment; commercially available instruments are fabricated by a number of manufacturers [219]. Semiconductor heterostructures are used as a Hall microprobe with a high-mobility 2D electron gas in GaAs/AlGaAs [220], InAlSb/InAsSb/InAlSb [221], as well as Bi [222] and graphene [223]. For example, in Ref. [220], a Hall microscope is described with a field sensitivity of ~ 0.1 G and a spatial resolution of ~ 0.35 μm, whereas Ref. [224] describes a vector magnetometer with a 1×1 μm GaAs sensor, providing a spatial resolution of ~ 700 nm.

5.3.4 Scanning SQUID magnetometers. The first scanning SQUID magnetometer (SSM), or SQUID microscope, was developed in 1992 [225]. The operational principles of SQUID as a magnetic field sensor are described in detail in textbooks [226, 227]. The typical SSM design includes a scanning module with a console, which carries a micro-SQUID. In contrast to MFM, where the spatial distribution of the magnetic field is deduced from the force acting between the probe and the sample, in an SSM the magnetic field is measured with a superconducting pickup coil of the SQUID. Various designs of SSMs are described in review articles [228, 229], and the operation theory and data interpretation can be found in [230].

To achieve a high spatial resolution, direct current SQUIDs (DC SQUIDs) are the most suitable. Their pickup loop ($\sim 1-10$ μm) and the SQUID sensor itself are fabricated using the electron-beam lithography technique. The threshold sensitivity is determined by the SQUID noise level and the effective area of the pickup loop. For a typical noise level $2 \times 10^{-6}\Phi_0$ Hz$^{-1/2}$ and the loop area 7 μm^2, the noise level is 10^{-6} G Hz$^{-1/2}$. In practical SSM devices [231, 232], a spatial resolution of ~ 20 nm and the lowest detected magnetic flux $(10^{-3}-10^{-5})\Phi_0$ Hz$^{-1/2}$ was achieved for the SQUID pickup loop diameter ~ 1 μm.

Scanning SQUID microscopes are also available as commercial products [233], in particular, the SM-77 SQUID microscope, designed and fabricated at the Faculty of Physics, Moscow State University [234].

5.4 Comparison of the local magnetometry methods

Each of the local magnetometry methods listed above has its own merits and drawbacks [235]: the MFM has a high spatial resolution (up to $10-100$ nm) and can operate in a wide range of temperatures. SQUID magnetometers have a very high sensitivity (up to 10^{-15} T Hz$^{-1/2}$), but the worst spatial resolution ($\sim 0.3-10$ μm) and are capable of working only at low temperatures. Hall microscopes have an intermediate resolution ($\sim 0.3-1$ μm). NV magnetometers are characterized by a good combination of spatial resolution ($\sim 1-10$ nm), high magnetic sensitivity, and a wide range of temperatures. For all the devices, however, there is a compromise between the accessible threshold sensitivity and spatial resolution: for example, for NV magnetometers, the sensitivity increases sharply, up to a few pT Hz$^{-1/2}$ in using an NV-center ensemble (albeit with a loss in spatial resolution) in a 10^{-3} mm^3 volume [176, 183, 236].

6. Results of physical investigations

In this section, we briefly consider several key physical results obtained from measurements of electron magnetization.

6.1 Orbital magnetization of two-dimensional electron systems

Besides the very fact of observing dHvA oscillations in a 2D electron system in experiments [7, 8, 45, 46], the theory of magnetooscillations was tested for 2D [54, 55, 95, 96] and quasi-one-dimensional [237] systems. In Refs [47], electron magnetization was probed in the regime of the fractional quantum Hall effect.

Already in 1980–1990 measurements of orbital magnetization were used to obtain information on the disorder-induced Landau level broadening, the level shape, the density of states within the gaps between the levels, the character of electron scattering [4, 27, 238–240], the spatial inhomogeneity of the electron distribution, and its effect on oscillation damping [241]. Furthermore, magnetization measurements in 2D systems were used to study breakdown mechanisms and current 'pinching' in the QHE regime. Related contactless magnetic measurements for studies of the orbital magnetization and charge transport are considered in detail in review [4].

Orbital magnetization measurements are also commonly used to estimate the residual resistance in the QHE regime. The results of these measurements are briefly described in Section 6.1. The absolute amplitude of dHvA oscillations and inter-electron exchange interaction at neighboring Landau levels were measured using various magnetometry methods [104, 242, 243]. The results of these measurements were compared with theoretical calculations [243, 244] of the oscillation amplitude enhancement due to the many-body effects of electron–electron interaction (the so-called 'inter Landau level interaction').

Recently, in connection with intensive studies of quasi-2D high-temperature superconductors and topological insulators, measurements of magnetization oscillations have become even more widespread.

6.1.1 Hysteresis nonstationary recharging effects in the QHE regime. With a growing $\hbar\omega_c/(k_B T)$ ratio, the diagonal components of resistivity and conductivity in the QHE regime decrease exponentially and then saturate. The residual dissipative resistivity is an important parameter, both for clarifying the transport mechanism in the gapped state and for estimating the accuracy of reproducing quantized Hall resistance in the Ohm standards [111, 245]. The residual resistance is so tiny, however, that it can hardly be measured with contact-type transport techniques; besides, the area in the vicinity of heavily doped contacts introduces excessive electron scattering. For this reason, the possibility of contactless estimation of the true residual resistance offered by magnetometry is very valuable.

Nonstationary effects in recharging a 2D layer in the QHE have been found in Ref. [50] in measurements of the chemical potential μ variations for the Si MOS structure, and, independently, in Ref. [6] in measurements of magnetization oscillations at the GaAs–AlGaAs heterojunction. Figure 21 shows that the hysteresis effect in the chemical potential is observed when varying both $\delta\mu(H) = \int(\partial\mu/\partial H)\,\mathrm{d}H$ and the electron density $\delta\mu(n) = \int(\partial\mu/\partial n)\,\mathrm{d}n$. The phenomenological interpretation of the observed hysteresis, suggested in [50], was confirmed in subsequent studies; however, the microscopic origin of the effect remained a subject of debate for a long time.

The physical picture of nonstationary eddy current excitation is simple at first glance: under a magnetic field or electron density changes, in the QHE regime, the relation $n = i \times n_H$ must hold between the number of electrons n and the flux quantum $n_H = \Phi/\Phi_0$ (where i is an integer). This process requires a recharging current to flow in the 2D layer. The Lorentz forces divert the charges coming into the 2D layer, thereby causing eddy current excitation. The decay time of the eddy currents $\sim C/\sigma_{xx}$ tends to infinity as $\sigma_{xx} = \rho_{xx}/\rho_{xy}^2 \to 0$. In practice, however, ρ_{xx} saturates below a certain temperature; the corresponding saturation of the decay time allows determining an important parameter, the true value of the dissipative residual resistance of the 2D system in the QHE regime, undistorted by contact effects.

Nonstationary recharging currents were studied in the integer QHE [4, 240, 246, 247] and fractional QHE [248] regimes. In addition to macroscopic 2D structures, nonstationary eddy currents were also observed in quantum dots in the QHE regime [249].

The dynamics of eddy current decay were measured in many studies [6, 9, 50, 247]. For a GaAs–AlGaAs heterojunction, the decay time was estimated as 300 s at $T = 400$ mK in Ref. [6]. In a more detailed investigation of the eddy current decay dynamics performed at a temperature of 40 mK in the QHE $\nu = 4$ state [9], the decay was found to be consistent with the exponential function whose argument strongly varies with temperature, as expected for hopping-type conductivity in the

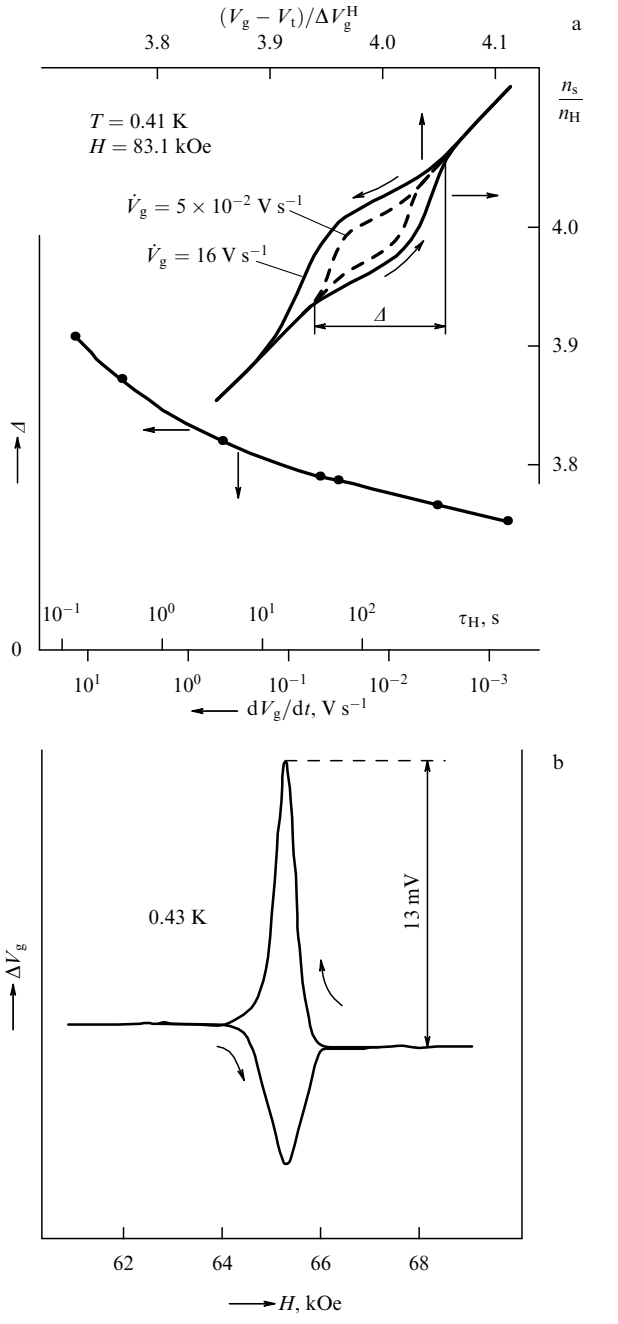

Figure 21. Hysteresis variation in the chemical potential with changes in the electron density in the MOS structure (a), and the magnetic field (b), quoted from Ref. [50]. Top right: the hysteresis loop for two dV_g/dt values. Bottom left: the dependence of the hysteresis loop width on the rate dV_g/dt.

QHE regime. However, for deeper resistance minima $\nu = 2$ and 1, a more complex picture was found.

For the $\nu = 2$ state, eddy currents initially decay fast, with a characteristic time $\tau_1 \approx 40$ s, which is related to a breakdown of the QHE by eddy currents. Then, a slower process starts developing with a characteristic time $\tau_2 \approx 3.6$ h. Taking the τ_2 value as an estimate of the true decay time in the low-current regime, in Ref. [9], an estimate was obtained for the residual resistance at $T = 40$ mK: $\rho_{xx}^{\min} \sim 10^{-14}$ Ωm/$\square$ for the $\nu = 2$ state and $\rho_{xx}^{\min} \sim 10^{-11}$ Ωm/$\square$ for the $\nu = 4$ state. A similar estimate was obtained in Ref. [50] for the Si-MOS structure ($\nu = 4$, $T = 0.3$ K): $\rho_{xx}^{\min} \approx 10^{-11}$ Ωm/$\square$, and in [7] for the GaAs/AlGaAs heterojunction.

Thus, for a typical capacitance of 1 nF for a gated 2D structure, the characteristic recharging time $\tau = C/\sigma_{xx} = C\rho_{xy}^2/\rho_{xx}$ lies in the range from $\sim 10^4$ s [7] to $\sim 10^{10}$ s [9, 50]. These figures are quoted here to illustrate the time scale of the effect; of course, they depend on the temperature, the relevant energy gap in the electron spectrum, and the Landau level broadening [9].

Consequently, the giant resistance drop $\rho_{xx}^{\min}/\rho_{xy}$ by a factor of $\sim 10^{14} - 10^{17}$ in the QHE regime illustrates the empirical accuracy of reproducing the quantized resistance value in the Ohm standards [111, 245]. Another practical application of the sharp peaks of the nonstationary magnetic response under recharging in the QHE regime is the control of homogeneity of the 2D system. Indeed, because ρ_{xx} increases exponentially sharply with deviation from the middle point between the Landau levels, the hysteresis effects occupy a narrow range in the field or in density; the sharp response thereby uncovers the presence of domains with different concentrations of delocalized states in the 2D layer.

Already in the first paper [50], it was pointed out that the eddy currents can flow locally around macroscopic localized areas in a smooth fluctuating potential landscape, or along the real sample edges, leading to a stored inductive or capacitive energy. This issue was discussed in a number of papers [9, 246], until the profile of the nonstationary current distribution was measured experimentally using an electrometer with submicron spatial resolution [250, 251]. It was found that, indeed, the eddy current is concentrated mainly along the 2D system perimeter, a few microns from the 2D sample edges. This conclusion is consistent with the magnitude of the eddy current estimated from direct measurements using a torque magnetometer [252].

In spite of the apparently exhaustive answer from spatially resolved experiments, the eddy current distribution seems to be more complex [252]. The induced eddy currents circulate along the equipotential lines in the presence of potential fluctuations, forming numerous current loops with various areas. Each current loop decays at its own rate, related to its capacitance and conductivity. At the end of the decay, for the remaining single loop, the decay should occur exponentially with time. These arguments [4], though plausible, are not fully consistent with the fact that the exponential law was not observed in the experiments even after 24 h.

Finally, nonstationary currents were used as a valuable tool for contactless measurements of the breakdown currents in the QHE regime and of the charge and current distribution in the sample in the QHE regime, and also to estimate energy gaps in the electron spectrum [10, 252–254] — issues interesting for physics and important for the QHE metrology.

6.1.2 Structure of the density of states in the QHE regime. Measurements of the orbital electron magnetization were used in a number of studies to clarify the energy structure of the density of states $D(E)$ at the Landau levels, in particular in the gaps between the levels. According to the semiclassical theory, for an ideal 2D gas with zero width of the Landau levels, $\Gamma = 0$, magnetization must vary with the field in a sawtooth fashion, with the amplitude μ_B^* per electron and with a zero width of jumps in the field [107, 255]. A similar dependence was observed experimentally in high-mobility GaAs/AlGaAs heterojunctions [13, 23, 238].

To account for the disorder effect, in the case of isotropic elastic scattering and an ideal noninteracting electron gas, the density of states is usually described by a Gaussian or Lorentzian function [4, 7, 255]:

$$D_{\mathrm{LL}}^{\mathrm{G}}(E) \propto \frac{1}{\pi l_B^2}\frac{1}{\sqrt{2\pi}\Gamma}\sum_{N=0}^{\infty}\exp\left(-\frac{(E-E_N)^2}{2\Gamma^2}\right),$$
$$D_{\mathrm{LL}}^{\mathrm{L}}(E) \propto \frac{1}{\pi l_B^2}\sum_{N=0}^{\infty}\frac{\Gamma}{\left[(E-E_N)^2+\Gamma^2\right]}, \qquad (18)$$

where $l_{\mathrm{B}} = \sqrt{\hbar/eB}$ is the magnetic length, $E_N = (N+1/2)\hbar\omega_{\mathrm{c}}$ is the energy of the Nth Landau level, and Γ is level broadening.

It is well known, however, that the experimentally measured density of states deviates from the Gaussian dependence. In many papers, this deviation is phenomenologically described by introducing a background density of the in-gap states [23] between the Landau levels:

$$D(E) = \zeta\frac{m^*}{\pi\hbar^2} + (1-\zeta)\frac{2eB}{\pi h}D_{\mathrm{LL}}(E), \qquad (19)$$

where the first term describes the energy-independent density of states and ζ is a fitting parameter.

In Refs [23, 24, 239, 256], the measured oscillations of the thermodynamic parameters for a 2D electron system were compared with theory. The shape of the measured quantum oscillations in [123, 257] turned out to be described best using the Lorentzian distribution with field-independent Γ, and using ζ as an adjustable parameter. In contrast, in Ref. [23, 24], the authors successfully approximated the shape of magnetization oscillations (and the shape of the electron specific heat in Ref. [258]) by using the Gaussian distribution with $\Gamma \propto \sqrt{B}$ and with constant ζ. Finally, in Ref. [239], the oscillations were found to be equally well described with Gaussian and Lorentzian distributions, with field-independent Γ.

This apparent inconsistency of experimental results, in fact, finds an explanation in theoretical calculations for a smooth random potential [259, 260], according to which, in weak fields, the Landau level width must vary with the field as $\sqrt{B}$, whereas in a strong field it must saturate and become field independent.

The empirically determined nonzero width of magnetization jumps δB, i.e., the nonzero 'background' density of states in the QHE regime, is often attributed to in-gap states, belonging to a separate reservoir of electron states, outside the 2D system. In the framework of such an approach, from the width of the jump we can estimate the concentration of such states by describing it phenomenologically with the same parameter ζ, $n_{\mathrm{gap}} = n\delta B/B$. In particular, in Ref. [13, 23], the authors estimated $n_{\mathrm{gap}}/n \sim 2-3\%$ for $\nu = 2$ in a field of 12 T. However, such a huge value, $\zeta = 2-3\%$ [13, 23], and even $\zeta = 49\%$ [91], makes this hypothesis unphysical in our opinion.

A quite similar idea of the existence of an electron reservoir outside the 2D system, which the electrons can enter and leave depending on the Fermi level position in the gap, was discussed at an earlier stage of QHE studies. To test this assumption, in Ref. [261] measurements were performed of the charge coming in to the MOS structure. It was found experimentally that this charge coincides with the charge of the 2D layer within an experimental accuracy of $< 2\%$; in other words, reservoirs of such a huge capacity are missing in the Si-MOS structure.

In Refs [262, 263], an attempt was made to link the background density of states with statistical fluctuations of the spatial distribution of electrons. Another interpretation of the puzzling background density of states was suggested in [102, 115, 264]: the authors described the experimentally observed density of states using a Gaussian distribution with the width $\Gamma(\nu)$ depending on the filling factor in an oscillatory fashion. Such an interpretation is consistent with the concept of nonlinear screening and also with experimentally observed oscillations of the Landau level width [102, 115].

6.1.3 Renormalization of the oscillation amplitude of orbital magnetization by interelectron interaction. As described above, the energy spectrum of a 2D system in a quantizing perpendicular magnetic field B consists of δ-like discrete levels (see Eqn (12)). The magnetization per electron in a 2D system $\partial M/\partial n = -\partial E/\partial B$, is

$$\frac{\partial M}{\partial n} = -\sum_N \mu_{\mathrm{B}}\left[\frac{m}{m^*}(2N+1) \pm \frac{1}{2}g^*\right]. \qquad (20)$$

This relation is satisfied in all field intervals between the integer numbers of level fillings ($\nu = n/\Phi_0$ is an integer and $\Phi_0 = hc/e$ is the flux quantum), where the magnetization experiences a jump. The amplitude of the jumps equals $2\mu_{\mathrm{B}}(m/m^*)$ for cyclotron splittings (i.e., transitions $\nu \to \nu \pm 1$), or $g^*\mu_{\mathrm{B}}$ for Zeeman splittings between levels with oppositely directed spins.

A nonzero temperature broadens the step-like changes in the filling function at the Fermi level, which leads to broadening of the interval of jump-like changes in $\mu(H)$. Disorder, in turn, causes broadening of the initially δ-like Landau energy levels. As a result, both factors, temperature and disorder, cause a diminishing of the jump amplitude $\partial M/\partial n$.

When e–e interaction is taken into account, the effective mass and g-factor vary due to the Fermi-liquid renormalization, and the jump amplitude must differ from the free-electron value. In a quantizing magnetic field, the renormalization (by virtue of the so-called 'inter Landau level interaction' or 'level repulsion') leads to the enhancement of the jump amplitude. Such an enhancement of the energy level splitting in the interacting 2D electron system was observed experimentally and predicted theoretically [244].

Figure 22a shows the measured chemical potential for a 2D electron system in Si as a function of the perpendicular magnetic field B (upper curve) [105, 242]. The sharp jump of $\mu(B)$ at about 10 T corresponds to the Fermi level transition from the second to the third energy level. For the Fermi level location in the energy gap, i.e., in the integer QHE regime, as was described above, the resistance of the 2D system decays exponentially, its recharging under such conditions being accompanied by eddy current excitation considered in Section 6.1.1. For this reason, the $\mu(B)$ behavior in Fig. 22 in this range of fields is schematically interpolated with a dashed-dotted line.

Figure 22b shows the $\mu(B)$ dependence [105] calculated for a noninteracting 2D electron gas at $T = 0$ in the absence of disorder, and also for typical disorder-induced Landau level broadening. We can see that the slope of the measured dependence (i.e., magnetization per electron) $\partial\mu/\partial B = -\partial M/\partial n$ for $\nu < 2$ is about a factor of two greater than the maximum possible slope, ($\partial M/\partial n = \mu_{\mathrm{B}}$) for a noninteracting

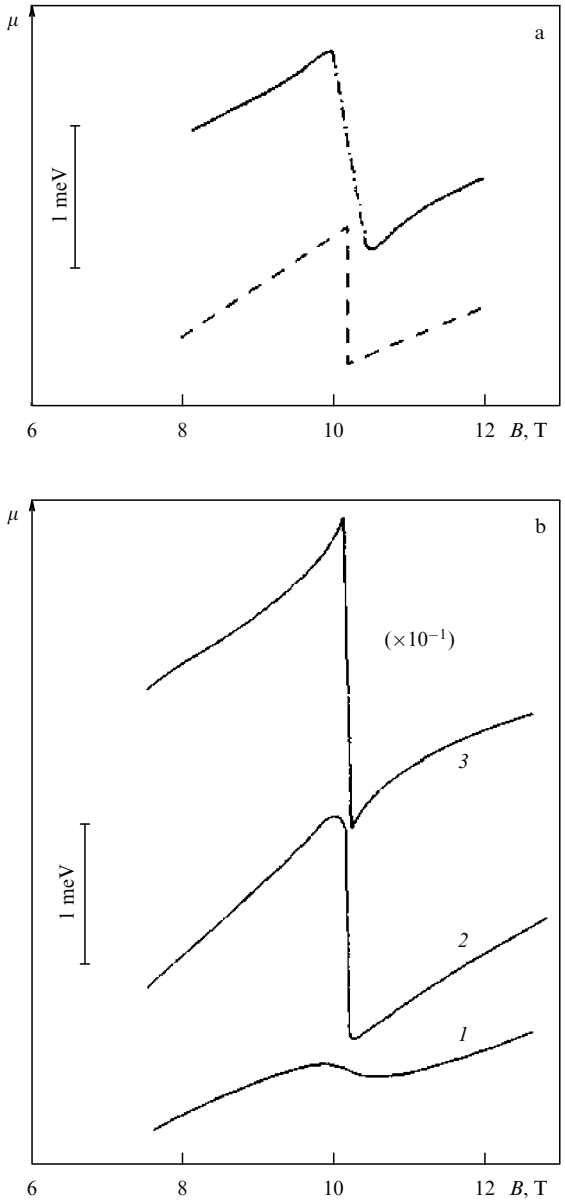

Figure 22. (a) Chemical potential (solid line) as a function of the field B for a jump at $\nu = 2$, from Ref. [105]. Temperature $T = 1.3$ K, density of electrons $n = 5 \times 10^{11}$ cm^{-2}. Dashed curve shows the calculated $\mu(B)$ dependence for a 2D system of noninteracting electrons at $T = 0$ and in the absence of disorder. (b) Theoretical $\mu(B)$ dependence for two values of T and for the dimensionless Coulomb interaction contribution α [105]: $\alpha = 0$, $T = 0$, and $T = 1.5$ K, $\alpha = 0$, 0.06, and 0.782 (curves *1*, *2*, and *3*), respectively. The last value corresponds to the classical Coulomb interaction.

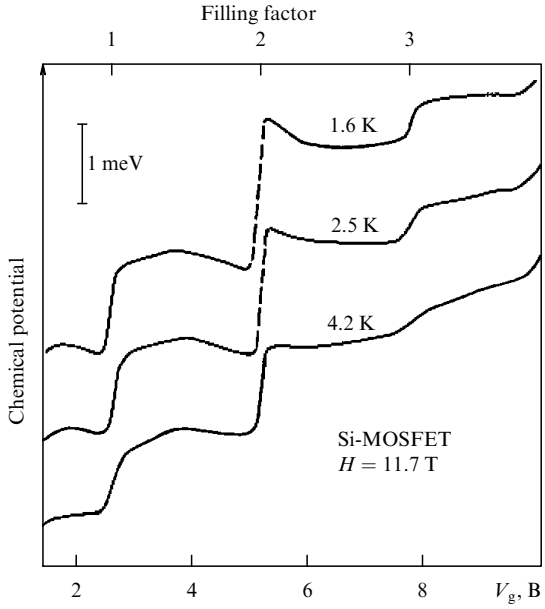

Figure 23. Chemical potential dependence on electron density (controlled via the gate voltage V_g), measured for three temperatures (Ref. [242]).

electron gas. The steep slope originates from the contribution of electron–electron interaction, which also enters the inverse thermodynamic density of states (thermodynamic compressibility) $(\partial n/\partial\mu)^{-1}$ and determines its negative value. This effect was predicted by Efros [265] and experimentally observed in Refs [105, 266, 267].

Qualitatively, the 'negative compressibility' is clearly seen in Fig. 23 as well, where the chemical potential for a 2D electron system is shown versus the electron concentration, measured in a constant magnetic field [242]. Instead of the anticipated (for a noninteracting system) step-like $\mu(n)$ dependence with jumps and with the related positive slope $\mathrm{d}\mu/\mathrm{d}n$ in the interval between them, we can clearly see intervals with $\mathrm{d}\mu/\mathrm{d}n < 0$. These wings with a negative slope on both sides of the integer fillings ν are direct evidence of a negative contribution to the chemical potential due to interelectron interaction (i.e., negative compressibility). The renormalized amplitude of the dHvA oscillations was measured in a number of studies [243] and was found to be in qualitative agreement with theory.

6.2 Spin magnetization of electrons

The problem of electron spin magnetization measurements in 2D systems became topical in the 2000s, in connection with investigations of interelectron correlation effects. The many-body effects become progressively stronger in 2D systems as the electron concentration was decreased, which, in turn, became possible as a result of the improvement in the quality of 2D structures. Commonly, the interelectron interaction is quantitatively characterized by a dimensionless ratio of the potential interaction energy and the kinetic Fermi energy, r_s [107].

To study the effect of electron–electron correlations on the spin degree of freedom, numerous experiments were performed using direct thermodynamic methods as well as indirect (i.e., based on theoretical models) transport methods; a brief description and the main results are given below.

6.2.1 Spin susceptibility renormalization determined from oscillatory and monotonic transport. Figure 24a shows the main result summarizing measurements of $\chi^*/\chi_b \propto g^*m^*/(2m_b)$ for a 2D electron system in Si-MOS structures [89–91, 94]. We can see that as a result of electron–electron interaction, the susceptibility $\chi^* \propto g^*m^*$ increases monotonically with r_s (i.e., as the density decreases) by a factor of ~ 5, although it remains finite in the explored range of electron densities.

From the measurements of $\chi^*/\chi_b = g^*m^*/2m_b$, together with the renormalized effective mass $m^*(r_s)$, we can extract the renormalized g^*-factor and hence estimate the lowest-order Fermi liquid coupling parameter F_0^σ. The effective mass

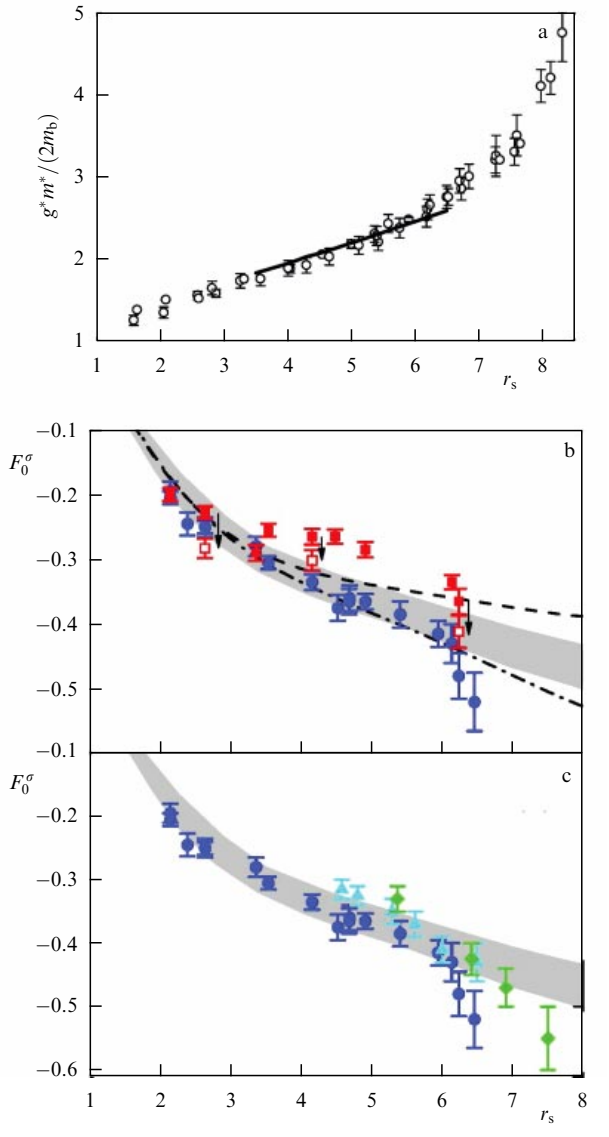

Figure 24. (a) Spin susceptibility χ^*/χ_b dependence on r_s, from [94] (dots). Solid lines — data from [90]. (b) $F_0^\sigma(r_s)$ data obtained from the $\sigma(T)$ and $\sigma(B)$ fitting with a theoretical dependence [68, 69]. Dashed line — $F_0^\sigma(r_s)$ values extracted from SdH [94] measurements and using the Lifshitz–Kosevich theory [54]; dashed-dotted curve — empirical approach from [94]. The shadowed corridor represents $F_0^\sigma(r_s)$ with experimental uncertainties obtained from SdH data fitting [96] with the theory in Ref. [94]. (c) F_0^σ values determined from $\sigma(T, B = 0)$; various symbols correspond to the data from [71], as well as from [70, 73], recalculated as described in [71].

m^* can be found from the temperature dependence of quantum oscillations. Figure 24b shows the resulting $F_0^\sigma(r_s)$ dependence obtained from quantum oscillations; the results of Ref. [91] also agree with the data in Fig. 24b. As can be seen from Fig. 24c, the $F_0^\sigma(r_s)$ values deduced from SdH oscillations reasonably well agree with the results obtained from fitting the $\sigma(T, B = 0)$ temperature dependence by the method considered in Section 3.1.2.

Finally, Fig. 25, taken from Ref. [84], summarizes the results for 2D electron and hole systems; it demonstrates the impact of the character of disorder, clearly breaking the data into two groups, for short-range and long-range (compared with the Fermi wave length $\lambda_F \sim 100$ Å) potential fluctuations, which are described by respective theories in [68, 69] and [82, 83].

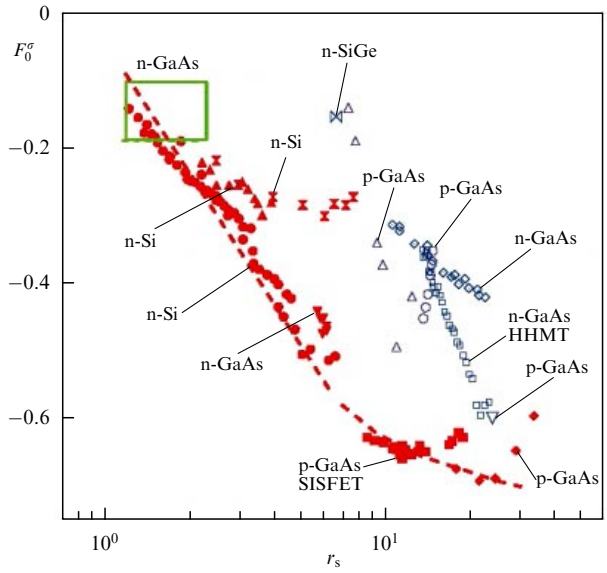

Figure 25. (Color online.) Summary of F_0^σ values, from Ref. [84]. The red filled symbols are for induced 2D systems, blue outline symbols are for n- and p-type 2D systems in various materials. The green box surrounds the range of F_0^σ anticipated for 2D n-GaAs systems according to the theory of smooth potential screening [84]. The dashed line is shown for clarity. HHMT — High Hole Mobility Transistor, SISFET — Semiconductor–Insulator–Semiconductor Field Effect Transistor.

For higher r_s values, F_0^σ tends to saturation at the level of about -0.8; as a result, the Stoner instability expected for $F_0^\sigma = -1$ appears to be unattainable for all the studied 2D material systems. Another reason for the attainability of the magnetic transition in a single-phase 2D system is discussed in Section 6.2.2.

6.2.2 Spin magnetization and susceptibility from thermodynamic measurements. The method of $d\mu/dB$ thermodynamic measurements was described in Section 4.3. Using this method, and by modulating the perpendicular, $B_\perp$, rather than the parallel magnetic field, in Ref. [119] the renormalized g-factor and cyclotron mass m^* were measured for a 2D electron system in Si; evidently, the results include orbital effects of interelectron interaction. To probe purely spin effects free of any orbital contribution, measurements in Ref. [117, 118] were performed in a magnetic field aligned strictly parallel to the 2D plane. These results obtained in a strong magnetic field $B_\parallel$ enable us to detect features expected for the full spin polarization (see Fig. 26).

In a partially polarized system, the electrons at the Fermi level have equal densities of states for both spin projections and contribute almost nothing to the magnetization dM/dn. Starting from the field of complete spin polarization, the dM/dn value should sharply increase from 0 to $-\mu_B$, as is schematically shown by the bold dashed line in Fig. 26a. A qualitatively similar behavior was observed in experiments [117, 118, 268] and is shown in Fig. 26a.

Most of the measurements with this technique were performed in [117, 118] in the regime of strong fields $g\mu_B B \gg k_B T$, which evidently 'cuts off' the dM/dn temperature dependence. In subsequent thermodynamic measurements [120] performed with improved sensitivity, a different behavior of $\partial M/\partial n$ was observed in weak fields ($g\mu_B B < k_B T$), as shown in Fig. 26b. At high electron densities, $\partial M/\partial n$ is negative [120], as expected for the Fermi-

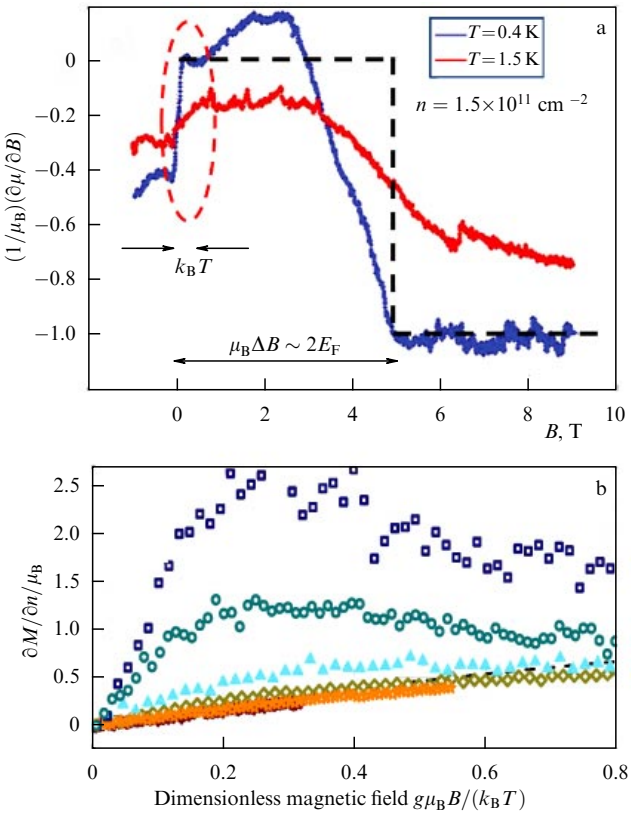

Figure 26. (Color online.) (a) Typical $\partial\mu/\partial B = -\partial M/\partial n$ dependence on the magnetic field for 2D electron system in an Si-MOS structure with a density of 1.5×10^{11} cm^{-2}. Horizontal arrows mark the characteristic field ranges corresponding to the normalized doubled Fermi energy, $\Delta B = 2E_F/(g\mu_B)$, and to the normalized temperature, $\delta B = k_B T/(g\mu_B)$. The dashed ellipse encloses a weak field region, magnified in the lower panel. (b) dM/dn weak field dependence plotted versus the normalized magnetic field $b = g\mu_B B/(k_B T)$ for a carrier density of 0.5×10^{11} cm^{-2} at various temperatures ($T = 0.8$, 1.2, 1.8, 4.2, 7, 10, 24 K, from top down).

liquid because of the effective mass renormalization $\partial m^*/\partial n < 0$.

At low densities, $\partial M/\partial n$ becomes positive and in all cases is much greater than expected for the Pauli spin susceptibility. When the field increases (while still being smaller than the temperature, $g\mu_B B < k_B T$), dM/dn sharply increases and exceeds the Bohr magneton by more than a factor of two at low temperatures (Fig. 26b).

Such behavior of $\partial M/\partial n(B)$ is reminiscent of the dependence anticipated for free spins, $\partial M/\partial n = \mu_B \tanh b$, where $b = \mu_B B/(k_B T) \ll 1$ is the dimensionless magnetic field. However, the fact that $\partial M/\partial n$ exceeds the Bohr magneton points to a ferromagnetic ordering of the electron spins. The magnetization curves $\partial M/\partial n$ (Fig. 26b) saturate in the field $b \approx 0.25$, signaling that the particles that respond to the field modulation have spins $\sim 1/(2b) \approx 2$, rather than 1/2.

Thus, the results in Ref. [120] evidence the emergence of a two-phase state in the 2D system consisting of a paramagnetic Fermi liquid and ferromagnetic domains (so-called 'spin droplets') with the total spin ~ 2, comprising $\gtrsim 4$ electrons. It seems likely that the formation of a two-phase state is more favorable than a transition to the uniform ferromagnetic state, which is, in addition, forbidden by the Mermin–Wagner theorem at $T \neq 0$. In the considered case, the easily orientable 'nanomagnets' remain as the minority phase in the majority Fermi-liquid phase, even though the dimensionless conductance of the 2D system $k_F l \gg 1$. Such conductance was commonly considered a criterion of the well-defined Fermi-liquid state. We note that the two-phase state often occurs in interacting electron systems in the vicinity of phase transitions, expected for a uniform state [269–271].

7. Conclusion

Measurements of the magnetic properties of nonmagnetic or weakly magnetic materials always represented a topical task, relevant for both practical material applications and physical studies. The doubtless advantage of magnetometry is related to the thermodynamic character of measurements, which in many cases provides simple and reliable interpretations of the results. Experimental methods of the magnetic measurements are continuously being improved, especially since the end of the 20th century. Here, we have considered various methods of magnetometry and their evolution in the last 50 years. As a result of their development, dozens of outstanding laboratory magnetometer designs appeared, followed by a large number of commercially available magnetometers and susceptometers.

The demand for magnetic measurements rose sharply at the beginning of the 1970s, related to the discovery and intensive studies of low-dimensional systems of electrons in semiconductor structures [107] and in organic crystals [270, 272, 273]. Low-dimensional electron systems manifest a rich novel physics in strong magnetic fields. Besides traditional transport and optical measurements, their study also requires thermodynamic, and particularly magnetic, measurements. Investigations of orbital magnetization of low-dimensional electron systems and nanostructures with a low number of electrons has required improving traditional designs and developing novel methods for magnetic measurements. Along with the discovery and studies of the integer and fractional quantum Hall effects, simultaneously performed magnetic measurements with 2D electron systems have led to a deeper understanding of the origin of these effects and properties of novel quasiparticles describing the fractional-charge states, composite quasiparticles consisting of electrons and flux quanta, and collective spin excitations in electron systems.

At the beginning of the 21st century, the problem of weaker effects of electron spin magnetization came to the forefront. This is related to the topical problem of understanding the properties of strongly correlated electron systems, searching for novel states of electron matter, and studying the effects of spin ordering and their interplay with superconducting paring, as well as with application in spintronics and quantum computations.

Finally, in recent years, new methods of magnetometry with spatial and temporal resolution have been developed. Local probing uses tools such as scanning magnetometers based on NV centers, SQUID magnetometers, scanning Hall magnetometers, and scanning atomic force microscopes. Time-resolved magnetometry enables studying magnetization dynamics during relaxation of the system between two quantum states. These methods have great potential because they are suited to magnetic measurements with more and more popular nanomaterials, nanostructures of topologically nontrivial matter, and optically controlled matter. The magnetometry methods with nm spatial resolution and temporal resolution are now rapidly being developed,

adapting to novel tasks, and will promote new discoveries and the accumulation of new knowledge, particularly in topical areas such as studies of quantum topological effects, novel quasiparticles (including Majorana fermions), living cells, microorganisms, and neurosystems. Scanning magnetic local microscopy suggests a unique possibility of noninvasive probing and visualization of the structure and dynamics of nano-objects.

Acknowledgments

The author is grateful to M E Gershenson, E M Dizhur, G Bauer, G Brunthaler, N Klimov, H Kojima, S V Kravchenko, A Yu Kuntsevich, L A Morgun, M Reznikov, D Rinberg, S G Semenchnisky, N Teneh, and V S Edel'man for their fruitful collaboration in developing experimental methods, performing measurements, discussing results, and writing the original papers. Financial support via the RFBR grant 18-02-01013 is acknowledged.

References

1. Griessen R *Cryogenics* **13** 375 (1973)
2. Vanderkooy J *J. Phys. E* **2** 718 (1969)
3. Foner S *Rev. Sci. Instrum.* **30** 548 (1959)
4. Usher A, Elliott M *J. Phys. Condens. Matter* **21** 103202 (2009)
5. Chechernikov V I *Magnitnye Izmereniya* (Magnetic Measurements) (Ed. E I Kondorskii) (Moscow: Izd. Mosk. Univ., 1969)
6. Eisenstein J P *Appl. Phys. Lett.* **46** 695 (1985)
7. Eisenstein J P et al. *Phys. Rev. Lett.* **55** 875 (1985)
8. Templeton I M *J. Appl. Phys.* **64** 3570 (1988)
9. Jones C L et al. *Solid State Commun.* **95** 409 (1995)
10. Matthews A J et al. *Phys. Rev. B* **70** 075317 (2004)
11. Matthews A J, Usher A, Williams C D H *Rev. Sci. Instrum.* **75** 2672 (2004)
12. Wiegers S A J et al. *Rev. Sci. Instrum.* **69** 2369 (1998)
13. Wiegers S A J et al. *Phys. Rev. Lett.* **79** 3238 (1997)
14. Schaapman M R et al. *Appl. Phys. Lett.* **81** 1041 (2002)
15. Bominaar-Silkens I M A et al. *New J. Phys.* **8** 315 (2006)
16. Schaapman M R et al. *Phys. Rev. B* **68** 193308 (2003)
17. Pudalov V M, Semenchinskii S G *Instrum. Exp. Tech.* **21** 1065 (1978); *Prib. Tekh. Eksp.* (4) 203 (1978)
18. Pudalov V M, Semenchinsky S G *J. Phys. Colloq.* **39** (C6) C6-1199 (1978)
19. Naughton M J et al. *Physica B* **246–247** 125 (1998)
20. Wilde M A et al. *Phys. Rev. B* **72** 165429 (2005)
21. Harris J G E et al. *Appl. Phys. Lett.* **75** 1140 (1999)
22. Schwarz M P et al. *Appl. Phys. Lett.* **76** 3564 (2000)
23. Schwarz M P et al. *Phys. Rev. B* **65** 245315 (2002)
24. Wilde M A et al. *Phys. Rev. B* **73** 125325 (2006)
25. Knobel R et al. *Phys. Rev. B* **65** 235327 (2002)
26. Harris J G E et al. *Phys. Rev. Lett.* **86** 4644 (2001)
27. Ruhe N et al. *Phys. Rev. B* **74** 235326 (2006)
28. Foner S *Rev. Sci. Instrum.* **27** 548 (1956)
29. Foner S *J. Appl. Phys.* **79** 4740 (1996)
30. Oliveira N F (Jr.), Foner S *Rev. Sci. Instrum.* **43** 37 (1972)
31. Mangum B W, Thornton D D *Rev. Sci. Instrum.* **41** 17646 (1970)
32. Bindilatti V et al. *Physica B* **194–196** 37 (1994)
33. Guertin R P, in *High-Pressure and Low-Temperature Physics* (Ed. C W Chu, J A Woollam) (New York: Plenum Press, 1978) p. 97
34. Guertin R P, Foner S, Missell F P *Phys. Rev. Lett.* **37** 529 (1976)
35. Reeves R *J. Phys. E* **5** 547 (1972)
36. Springford M, Stockton J R, Wampler W R *J. Phys. E* **4** 1036 (1971)
37. Johansson T, Nielsen K G *J. Phys. E* **9** 852 (1976)
38. Hoon S R, Willcock S N M *J. Phys. E* **21** 772 (1988)
39. Nizhankovskii V I, Lugansky L B *Meas. Sci. Technol.* **18** 1533 (2007)
40. Außerlechner U, Steiner W, Kasperkovitz P *Meas. Sci. Technol.* **7** 1574 (1996)
41. Bragg E E, Seehra M S *J. Phys. E* **9** 216 (1976)
42. Pudalov V M, Khaikin M S *Sov. Phys. JETP* **40** 1121 (1975); *Zh. Eksp. Teor. Fiz.* **67** 2260 (1974)
43. Pudalov V M *JETP Lett.* **19** 250 (1974); *Pis'ma Zh. Eksp. Teor. Fiz.* **19** 466 (1974)
44. Cryogenic Limited, London, UK, http://www.cryogenic.co.uk
45. Störmer H L et al. *J. Vac. Sci. Technol. B* **1** 423 (1983)
46. Haavasoja T et al. *Surf. Sci.* **142** 294 (1984)
47. Meinel I et al. *Phys. Rev. Lett.* **82** 819 (1999)
48. Meinel I et al. *Appl. Phys. Lett.* **70** 3305 (1997)
49. Fang F F, Stiles P J *Phys. Rev. B* **28** 6992 (1983)
50. Pudalov V M, Semenchinsky S G, Edelman V S *Solid State Commun.* **51** 713 (1984)
51. Shoenberg D *Can. J. Phys.* **46** 1915 (1968)
52. Shoenberg D, Templeton I M *Can. J. Phys.* **46** 1925 (1968)
53. Pippard A B, in *The Physics of Metals. I. Electrons* (Ed. J M Ziman) (Cambridge: Cambridge Univ. Press, 1969); Translated into Russian: in *Fizika Metallov* Vol. 1 *Elektrony* (Ed. J M Ziman) (Moscow: Mir, 1972)
54. Lifshitz I M, Kosevich A M *Sov. Phys. JETP* **2** 636 (1956); *Zh. Eksp. Teor. Fiz.* **29** 730 (1956)
55. Isihara A, Smrcka L *J. Phys. C* **19** 6777 (1986)
56. Das Sarma S, Hwang E H *Phys. Rev. B* **72** 035311 (2005)
57. Dolgopolov V T, Gold A V *JETP Lett.* **71** 27 (2000); *Pis'ma Zh. Eksp. Teor. Fiz.* **71** 42 (2000)
58. Shashkin A A et al. *Phys. Rev. Lett.* **87** 086801 (2001)
59. Pudalov V M et al. *Phys. Rev. Lett.* **88** 076401 (2002)
60. Broto J M et al. *Phys. Rev. B* **67** 161304(R) (2003)
61. Tutuc E, Melinte S, Shayegan M *Phys. Rev. Lett.* **88** 036805 (2002)
62. Gao X P A et al. *Phys. Rev. B* **73** 241315(R) (2006)
63. Lu T M et al. *Phys. Rev. B* **78** 233309 (2008)
64. Al'tshuler B L, Aronov A G, Zyuzin A Yu *JETP Lett.* **35** 16 (1982); *Pis'ma Zh. Eksp. Teor. Fiz.* **35** 15 (1982)
65. Zhang Y, Das Sarma S *Phys. Rev. Lett.* **96** 196602 (2006)
66. Vitkalov S A, Sarachik M P, Klapwijk T M *Phys. Rev. B* **65** 201106(R) (2002)
67. Sarachik M P, Vitkalov S A *J. Phys. Soc. Jpn.* **72** 53 (2003)
68. Zala G, Narozhny B N, Aleiner I L *Phys. Rev. B* **64** 214204 (2001)
69. Zala G, Narozhny B N, Aleiner I L *Phys. Rev. B* **65** 020201(R) (2001)
70. Vitkalov S A et al. *Phys. Rev. B* **67** 113310 (2003)
71. Klimov N N et al. *Phys. Rev. B* **78** 195308 (2008)
72. Pudalov V M et al. *Phys. Rev. Lett.* **91** 126403 (2003)
73. Shashkin A A et al. *Phys. Rev. B* **66** 073303 (2002)
74. Proskuryakov Y Y et al. *Phys. Rev. Lett.* **89** 076406 (2002)
75. Kvon Z D et al. *Phys. Rev. B* **65** 161304(R) (2002)
76. Olshanetsky E B et al. *Phys. Rev. B* **68** 085304 (2003)
77. Noh H et al. *J. Phys. Soc. Jpn.* **72** 137 (2003)
78. Noh H et al. *Phys. Rev. B* **68** 165308 (2003)
79. Savchenko A K et al. *Physica E* **22** 218 (2004)
80. Li L et al. *J. Phys. Soc. Jpn.* **72** 63 (2003)
81. Coleridge P T, Sachrajda A S, Zawadzki P *Phys. Rev. B* **65** 125328 (2002)
82. Gornyi I V, Mirlin A D *Phys. Rev. B* **69** 045313 (2004)
83. Gornyi I V, Mirlin A D *Phys. Rev. Lett.* **90** 076801 (2003)
84. Clarke W R et al. *Nat. Phys.* **4** 55 (2008)
85. Morgun L A, Kuntsevich A Yu, Pudalov V M *Phys. Rev. B* **93** 235145 (2016)
86. Li L et al. *Phys. Rev. Lett.* **90** 076802 (2003)
87. Kuntsevich A Yu, Morgun L A, Pudalov V M *Phys. Rev. B* **87** 205406 (2013)
88. Pudalov V M, Morgun L A, Kuntsevich A Yu *J. Supercond. Nov. Magn.* **30** 783 (2017)
89. Fang F F, Stiles P J *Phys. Rev.* **174** 823 (1968)
90. Okamoto T et al. *Phys. Rev. Lett.* **82** 3875 (1999)
91. Zhu J et al. *Phys. Rev. Lett.* **90** 056805 (2003)
92. Tsukazaki A et al. *Phys. Rev. B* **78** 233308 (2008)
93. Gershenson M E et al. *Physica E* **12** 585 (2002)
94. Pudalov V M et al. *Phys. Rev. Lett.* **88** 196404 (2002)
95. Martin G W, Maslov D L, Reizer M Yu *Phys. Rev. B* **68** 241309(R) (2003)
96. Adamov Y, Gornyi I V, Mirlin A D *Phys. Rev. B* **73** 045426 (2006)
97. Pudalov V M, Gershenson M E, Kojima H *Phys. Rev. B* **90** 075147 (2014)
98. Zhang Y, Das Sarma S *Phys. Rev. B* **72** 075308 (2005)
99. Zhang Y, Das Sarma S *Phys. Rev. Lett.* **97** 039701 (2006)

100. De Palo S et al. *Phys. Rev. Lett.* **94** 226405 (2005)
101. Tutuc E et al. *Phys. Rev. B* **67** 241309(R) (2003)
102. Pudalov V M, Semenchinskii S G, Édel'man V S *Sov. Phys. JETP* **62** 1079 (1985); *Zh. Eksp. Teor. Fiz.* **89** 1870 (1985)
103. Pudalov V M, Semenchinskii S G, Edel'man V S *JETP Lett.* **41** 325 (1985); *Pis'ma Zh. Eksp. Teor. Fiz.* **41** 265 (1985)
104. Pudalov V M, Semenchinskii S G *JETP Lett.* **44** 677 (1986); *Pis'ma Zh. Eksp. Teor. Fiz.* **44** 526 (1986)
105. Kravchenko S V et al. *Phys. Lett. A* **146** 535 (1990)
106. Kravchenko S V et al. *Phys. Rev. B* **42** 3741 (1990)
107. Ando T, Fowler A B, Stern F *Rev. Mod. Phys.* **54** 437 (1982)
108. Abrikosov A A *Introduction to the Theory of Normal Metals* (New York: Academic Press, 1972); Translated from Russian: *Vvedenie v Teoriyu Normal'nykh Metallov* (Moscow: Nauka, 1972)
109. Ashcroft N W, Mermin N D *Solid State Physics* (New York: Holt, Rinehart and Winston, 1976); Translated into Russian: *Fizika Tverdogo Tela* (Moscow: Mir, 1979)
110. Kittel Ch *Quantum Theory of Solids* (New York: Wiley, 1963); Translated into Russian: *Kvantovaya Teoriya Tverdykh Tel* (Moscow: Nauka, 1967)
111. Pudalov V M et al. *Sov. Phys. JETP* **62** 630 (1986); *Zh. Eksp. Teor. Fiz.* **89** 1094 (1985)
112. Nizhankovskii V I, Zybtsev S G *Phys. Rev. B* **50** 1111 (1994)
113. Zeller R T et al. *Phys. Rev. B* **33** 1529(R) (1986)
114. Nizhankovskii V I et al. *Sov. Phys. JETP* **63** 776 (1986); *Zh. Eksp. Teor. Fiz.* **90** 1326 (1986)
115. Semenchinskii S G *JETP Lett.* **41** 605 (1985); *Pis'ma Zh. Eksp. Teor. Fiz.* **41** 497 (1985)
116. Alekseevskii N E, Nizhankovskii V I *Sov. Phys. JETP* **61** 1051 (1985); *Zh. Eksp. Teor. Fiz.* **88** 1771 (1985)
117. Prus O et al. *Phys. Rev. B* **67** 205407 (2003)
118. Shashkin A A et al. *Phys. Rev. Lett.* **96** 036403 (2006)
119. Anissimova S et al. *Phys. Rev. Lett.* **96** 046409 (2006)
120. Teneh N et al. *Phys. Rev. Lett.* **109** 226403 (2012)
121. Reznikov M et al. *JETP Lett.* **92** 470 (2010); *Pis'ma Zh. Eksp. Teor. Fiz.* **92** 518 (2010)
122. Gritsenko V A *Phys. Usp.* **52** 869 (2009); *Usp. Fiz. Nauk* **179** 921 (2009)
123. Tupikov Y et al. *JETP Lett.* **101** 125 (2015); *Pis'ma Zh. Eksp. Teor. Fiz.* **101** 131 (2015)
124. Kuntsevich A Y et al. *Nat. Commun.* **6** 7298 (2015)
125. Kuntsevich A Yu et al. *JETP Lett.* **111** 633 (2020); *Pis'ma Zh. Eksp. Teor. Fiz.* **111** 750 (2020)
126. Dyakonov M I *Proc. SPIE* **7036** 70360R (2008)
127. Sinova J et al. *Rev. Mod. Phys.* **87** 1213 (2015)
128. Zvezdin A K, Davydova M D, Zvezdin K A *Phys. Usp.* **61** 1127 (2018); *Usp. Fiz. Nauk* **188** 1238 (2018)
129. Barabanov A F et al. *Phys. Usp.* **58** 446 (2015); *Usp. Fiz. Nauk* **185** 479 (2015)
130. Dyakonov M I, Perel V I *Phys. Lett. A* **35** 459 (1971)
131. D'yakonov M I, Perel' V I *JETP Lett.* **13** 467 (1971); *Pis'ma Zh. Eksp. Teor. Fiz.* **13** 657 (1971)
132. Averkiev N S, D'yakonov M I *Sov. Phys. Semicond.* **17** 393 (1983); *Fiz. Tekh. Poluprovodn.* **17** 629 (1983)
133. Bakun A A et al. *JETP Lett.* **40** 1293 (1984); *Pis'ma Zh. Eksp. Teor. Fiz.* **40** 464 (1984)
134. Tkachuk M N, Zakharchenya B P, Fleisher V G *JETP Lett.* **44** 59 (1986); *Pis'ma Zh. Eksp. Teor. Fiz.* **44** 47 (1986)
135. Hirsch J E *Phys. Rev. Lett.* **83** 1834 (1999)
136. Zhang S *Phys. Rev. Lett.* **85** 393 (2000)
137. Sinova J et al. *Phys. Rev. Lett.* **92** 126603 (2004)
138. Murakami S, Nagaosa N, Zhang S-C *Science* **301** 1348 (2003)
139. Murakami S, Nagaosa N, Zhang S-C *Phys. Rev. Lett.* **93** 156804 (2004)
140. Saitoh E et al. *Appl. Phys. Lett.* **88** 182509 (2006)
141. Valenzuela S O, Tinkham M *Nature* **442** 176 (2006)
142. Zhao H at al. *Phys. Rev. Lett.* **96** 246601 (2006)
143. Ehlert M et al. *Phys. Status Solidi B* **251** 1725 (2014)
144. Kato Y K et al. *Science* **306** 1910 (2004)
145. Wunderlich J et al. *Phys. Rev. Lett.* **94** 047204 (2005)
146. Stern N P et al. *Phys. Pev. Lett.* **97** 126603 (2006)
147. Sih V et al. *Phys. Rev. Lett.* **97** 096605 (2006)
148. Matsuzaka S, Ohno Y, Ohno H *Phys. Rev. B* **80** 241305(R) (2009)
149. Chang H J et al. *Phys. Rev. Lett.* **98** 136403 (2007)
150. Kato Y K et al. *Phys. Rev. Lett.* **93** 176601 (2004)
151. Valenzuela S O, Tinkham M *Nature* **442** 176 (2006)
152. Valenzuela S O, Tinkham M *J. Appl. Phys.* **101** 09B103 (2007)
153. Werake L K, Ruzicka B A, Zhao H *Phys. Rev. Lett.* **106** 107205 (2011)
154. Lou X et al. *Nat. Phys.* **3** 197 (2007)
155. Garlid E S et al. *Phys. Rev. Lett.* **105** 156602 (2010)
156. Brüne C et al. *Nat. Phys.* **6** 448 (2010)
157. Ehlert M et al. *Phys. Rev. B* **86** 205204 (2012)
158. Olejnik K et al. *Phys. Rev. Lett.* **109** 076601 (2012)
159. Valenzuela S O, Tinkham M *Appl. Phys. Lett.* **85** 5914 (2004)
160. Choi W Y et al. *Nat. Nanotechnol.* **10** 666 (2015)
161. Hankiewicz E M et al. *Phys. Rev. B* **70** 241301(R) (2004)
162. Mihajlović G et al. *Phys. Rev. Lett.* **103** 166601 (2009)
163. Kolwas K A et al. *Phys. Status Solidi B* **250** 37 (2013)
164. Balakrishnan J et al. *Nat. Phys.* **9** 284 (2013)
165. Datta S, Das B *Appl. Phys. Lett.* **56** 665 (1990)
166. Doherty M W et al. *Phys. Rep.* **528** 1 (2013)
167. Kraus H et al. *Sci. Rep.* **4** 5303 (2014)
168. Kraus H et al. *Nat. Phys.* **10** 157 (2014)
169. Fuchs P, Challier M, Neu E *New J. Phys.* **20** 125001 (2018)
170. Zhou T X, Stöhr R J, Yacoby A *Appl. Phys. Lett.* **111** 163106 (2017)
171. Pham L M et al. *New J. Phys.* **13** 045021 (2011)
172. Schloss J M et al. *Phys. Rev. Appl.* **10** 034044 (2018)
173. Barry J F et al. *Rev. Mod. Phys.* **92** 015004 (2020)
174. Maze J R et al. *Nature* **455** 644 (2008)
175. van Oort E, Manson N B, Glasbeek M *J. Phys. C* **21** 4385 (1988)
176. Taylor J M et al. *Nat. Phys.* **4** 810 (2008)
177. Balasubramanian G et al. *Nat. Mater.* **8** 383 (2009)
178. Ohno K et al. *Appl. Phys. Lett.* **101** 082413 (2012)
179. Maletinsky P et al. *Nat. Nanotechnol.* **7** 320 (2012)
180. Kleinlein J et al. *Microelectron. Eng.* **159** 70 (2016)
181. Appel P et al. *Rev. Sci. Instrum.* **87** 063703 (2016)
182. Rondin L et al. *Rep. Prog. Phys.* **77** 056503 (2014)
183. Hong S et al. *MRS Bull.* **38** 155 (2013)
184. Schirhagl R et al. *Annu. Rev. Phys. Chem.* **65** 83 (2014)
185. Jensen K, Kehayias P, Budker D, in *High Sensitivity Magnetometers* (Smart Sensors, Measurement and Instrumentation, Vol. 19, Eds A Grosz, M J Haji-Sheikh, S C Mukhopadhyay) (Cham: Springer Intern. Publ., 2017)
186. Wojciechowski A M et al. *Materials* **12** 2951 (2019)
187. Levine E V et al. *Nanophotonics* **8** 1945 (2019)
188. Boretti A et al. *Beilstein J. Nanotechnol.* **10** 2128 (2019)
189. Nizov V A "Ispol'zovanie NV-tsentrov v almaze dlya realizatsii novykh skhem magnitometrii" ("Application of NV-centers in diamond for novel magnetometry devices"), PhD Thesis (Phys.-Math.-Sci.) (Nizhny Novgorod: Institute of Applied Physics of the Russian Academy of Sciences, 2019)
190. Le Sage D et al. *Nature* **496** 486 (2013)
191. Fu R R et al. *Science* **346** 1089 (2014)
192. Glenn D R et al. *Nat. Meth.* **12** 736 (2015)
193. McGuinness L P et al. *Nat. Nanotechnol.* **6** 358 (2011)
194. Kuwahata A et al. *Sci. Rep.* **10** 2483 (2020)
195. Grinolds M S et al. *Nat. Phys.* **9** 215 (2013)
196. Jakobi I et al. *Nat. Nanotechnol.* **12** 67 (2017)
197. Waxman A et al. *Phys. Rev. B* **89** 054509 (2014)
198. Rondin L et al. *Nat. Commun.* **4** 2279 (2013)
199. Tetienne J-P et al. *Science* **344** 1366 (2014)
200. van der Sar T et al. *Nat. Commun.* **6** 7886 (2015)
201. Dussaux A et al. *Nat. Commun.* **7** 12430 (2016)
202. Martin Y, Wickramasinghe H K *Appl. Phys. Lett.* **50** 1455 (1987)
203. Yaminskii I V, Tishin A M *Russ. Chem. Rev.* **68** 187 (1999); *Usp. Khim.* **68** 187 (1999)
204. Cordova G, Lee B Y, Leonenko Z *NanoWorld J.* **2** (1) 10 (2016)
205. NT-MDT Spectrum Instruments, http://www.ntmdt.ru/
206. Stiller M et al. *Meas. Sci. Technol.* **28** 125401 (2017)
207. Li J W, Cleveland J P, Proksch R *Appl. Phys. Lett.* **94** 163118 (2009)
208. Rodríguez T R, García R *Appl. Phys. Lett.* **84** 449 (2004)
209. Schneiderbauer M, Wastl D, Giessibl F J *Beilstein J. Nanotechnol.* **3** 174 (2012)
210. Schwenk J et al. *Appl. Phys. Lett.* **104** 112412 (2014)
211. Schwenk J et al. *Appl. Phys. Lett.* **107** 132407 (2015)

212. Sidles J A *Appl. Phys. Lett.* **58** 2854 (1991)
213. Sidles J A, Garbini J L, Drobny G P *Rev. Sci. Instrum.* **63** 3881 (1992)
214. Sidles J A et al. *Rev. Mod. Phys.* **67** 249 (1995)
215. Züger O, Rugar D *Appl. Phys. Lett.* **63** 2496 (1993)
216. Grob U et al. *Nano Lett.* **19** 7935 (2019)
217. Rose W et al. *Phys. Rev. X* **8** 011030 (2018)
218. Zurich Instruments AG, https://www.zhinst.com/
219. Nanomagnetics Instrument, https://www.nanomagnetics-inst.com/
220. Chang A M et al. *Appl. Phys. Lett.* **61** 1974 (1992)
221. Bando M et al. *J. Appl. Phys.* **105** 07E909 (2009)
222. Sandhu A et al. *Jpn. J. Appl. Phys.* **43** 777 (2004)
223. Sonusen S et al. *Appl. Surf. Sci.* **308** 414 (2014)
224. Dede M, Akram R, Oral A *Appl. Phys. Lett.* **109** 182407 (2016)
225. Black R C et al. *Appl. Phys. Lett.* **62** 2128 (1993)
226. Clarke J, Braginski A I (Eds) *The SQUID Handbook* Vol. 1 *Fundamentals and Technology of SQUIDs and SQUID Systems* (Weinheim: Wiley-VCH, 2004)
227. Schmidt V V *The Physics of Superconductors*: *Introduction to Fundamentals and Applications* (Eds V V Schmidt, P Müller, A V Ustinov) (Berlin: Springer, 1997); Translated from Russian: *Vvedenie v Fiziku Sverkhprovodnikov* (Moscow: MTsNMO, 2000)
228. Kirtley J R, Wikswo J P (Jr.) *Annu. Rev. Mater. Sci.* **29** 117 (1999)
229. Kirtley J R et al. *IBM J. Res. Develop.* **39** 655 (1995)
230. Reith P, Wang X R, Hilgenkamp H *Rev. Sci. Instrum.* **88** 123706 (2017)
231. Vu L N, Van Harlingen D J *IEEE Trans. Appl. Supercond.* **3** 1918 (1993)
232. Kirtley J R et al. *Appl. Phys. Lett.* **66** 1138 (1995)
233. Attocube systems Inc., https://www.attocube.com/
234. PersT. Information Bulletin "Advanced technologies". Scanning SQUID microscope (SSM-77), http://perst.issp.ras.ru/Control/Inform/tem/HiTech/squid.htm
235. Kirtley J R *Rep. Prog. Phys.* **73** 126501 (2010)
236. Wolf T et al. *Phys. Rev. X* **5** 041001 (2015)
237. Wilde M A et al. *Physica E* **22** 729 (2004)
238. Wilde M A et al. *Phys. Status Solidi* **245** 344 (2008)
239. Zhu M et al. *Phys. Rev. B* **67** 155329 (2003)
240. Potts A et al. *J. Phys. Condens. Matter* **8** 5189 (1996)
241. Shoenberg D *Magnetic Oscillations in Metals* (Cambridge: Cambridge Univ. Press, 1984)
242. Kravchenko S V et al. *Phys. Rev. B* **42** 3741 (1990)
243. Meinel I et al. *Phys. Rev. B* **64** 121306(R) (2001)
244. MacDonald A H, Oji H C A, Liu K L *Phys. Rev. B* **34** 2681 (1986)
245. Krasnopolin I Ya, Pudalov V M, Semenchinskii S G *Instrum. Exp. Tech.* **30** 1275 (1988); *Prib. Tekh. Eksp.* (6) 5 (1987)
246. Faulhaber D R, Jiang H W *Phys. Rev. B* **72** 233308 (2005)
247. Kershaw T J et al. *New J. Phys.* **9** 71 (2007)
248. Watts J P et al. *Phys. Rev. Lett.* **81** 4220 (1998)
249. Pioro-Ladrière M et al. *Phys. Rev. B* **73** 075309 (2006)
250. Klaffs T et al. *Physica E* **22** 737 (2004)
251. Huels J et al. *Phys. Rev. B* **69** 085319 (2004)
252. Jones C L et al. *Solid State Commun.* **97** 763 (1996)
253. Kavokin K V et al. *Solid State Commun.* **134** 257 (2005)
254. Gething J D et al. *Int. J. Mod. Phys. B* **18** 3537 (2004)
255. Kukushkin I V, Meshkov S V, Timofeev V B *Sov. Phys. Usp.* **31** 511 (1988); *Usp. Fiz. Nauk* **155** 219 (1988)
256. Kuntsevich A Yu et al. *Nat. Commun.* **6** 7298 (2015)
257. Potts A et al. *J. Phys. Condens. Matter* **8** 5189 (1996)
258. Gornik E et al. *Phys. Rev. Lett.* **54** 1820 (1985)
259. Sa-yakanit V, Choosiri N, Glyde H R *Phys. Rev. B* **38** 1340 (1988)
260. Raikh M E, Shahbazyan T V *Phys. Rev. B* **47** 1522 (1993)
261. Pudalov V M, Semenchinskii S G, Edel'man V S *JETP Lett.* **39** 576 (1984); *Pis'ma Zh. Eksp. Teor. Fiz.* **39** 474 (1984)
262. Gudmundsson V, Gerhardts R R *Phys. Rev. B* **35** 8005 (1987)
263. Gerhardts R R, Gudmundsson V *Phys. Rev. B* **34** 2999(R) (1986)
264. Wang J K et al. *Phys. Rev. B* **38** 6174 (1988)
265. Efros A L *Solid State Commun.* **65** 1281 (1988)
266. Kravchenko S V, Pudalov V M, Semenchinsky S G *Phys. Lett. A* **141** 71 (1989)
267. Eisenstein J P, Pfeiffer L N, West K W *Phys. Rev. Lett.* **68** 674 (1992)
268. Dolgopolov V T *Phys. Usp.* **62** 633 (2019); *Usp. Fiz. Nauk* **189** 673 (2019)
269. Gorbatsevich A A, Kopaev Yu V, Tokatly I V *Physica C* **223** 95 (1994)
270. Kornilov A V et al. *Phys. Rev. B* **69** 224404 (2004)
271. Gerasimenko Ya A et al. *Phys. Rev. B* **89** 054518 (2014)
272. Lebed A (Ed.) *The Physics of Organic Superconductors and Conductors* (Springer Series in Materials Science, Vol. 110) (Berlin: Springer-Verlag, 2008)
273. Kornilov A V et al. *Phys. Rev. B* **65** 060404(R) (2002)